Structures 50 (2023) 1264–1284

Contents lists available at ScienceDirect

Structures

journal homepage: www.elsevier.com/locate/structures

Experimental and numerical study on behaviour of fibre reinforced lightweight hollow core slabs under different flexure to shear ratios

Sumit Sahoo, Chetharajupalli Veerendar, Nikesh Thammishetti, S Suriya Prakash *

Department of Civil Engineering, Indian Institute of Technology Hyderabad, Sangareddy 502285, India

ARTICLE INFO

Keywords:
Digital image correlation
Finite element analysis
Hollow core slab
Lightweight aggregate
Synthetic fibres

ABSTRACT

The current work explores the behaviour of fibre-reinforced lightweight hollow core slabs (FR-LWHCS) intending to develop sustainable construction solutions. The FR-LWHCS investigated in this work contains sintered fly ash aggregate (SFA) as coarse aggregate. Due to the use of SFA, the behaviour of LWHCS is expected to be different from the hollow core slabs (HCS) constructed using normal density concrete. FR-LWHCS are tested at different shear span to depth (a/d) ratios of 3.5, 7 and 10 to understand the shear and flexure behaviour. Twelve full-scale hollow core slab (HCS) specimens of 3400 mm length, 600 mm width, and 150 mm thickness are tested. FR-LWHCS consists of monofilament macro synthetic fibre dosages of 0.4 %, and 0.6 %, along with fibrillated micro fibre of 0.02 % dosage. The digital image correlation (DIC) technique is adopted to understand the strain profile on the HCS at different levels of loading. The numerical analysis is performed using a commercially available finite element software and is corroborated with experimental findings and parametric studies have been performed. Both LWHCS and normal HCS specimens failed in shear, flexural-shear and flexure modes at a/d ratios of 3.5, 7 and 10, respectively. The addition of fibres increased the peak load by 65 % compared to control LWHCS specimens tested at an a/d ratio of 3.5. The use of fibres increased strain energy absorption and changed the failure to less brittle mode at all a/d ratios. The fibre reinforced specimens have nearly 3.5 times, 2.5 times and 1.3 times the strain energy absorption of the control LWHCS when tested at a/d ratio 3.5, 7 and 10 respectively.

1. Introduction

A hollow core slab (HCS) is a precast concrete element containing voids along the span of the slab. The self-weight of slabs decreases due to the voids contributing to the reduction in construction cost [1]. HCS can be used as flooring elements, partition walls, spandrel members, bridge deck units, and roof deck systems. The voids in HCS can be used for electrical, water drainage, wiring, and air ducts for heating and cooling [2]. The self-weight of HCS can be further reduced by replacing the natural coarse aggregate with lightweight aggregates. The advantages of using lightweight aggregate concrete (LWAC) in HCS include light weight, high strength-to-weight ratio, good seismic performance, and structural integrity [3]. Also, it leads to a faster construction process and a decrease in material and transportation costs [4]. The lightweight aggregates used in structural applications are derived from various raw materials, including clays, clinker, shales, slates, fly ash, oil palm shell, coconut shell, pumice or blast-furnace slag [5]. Sintered fly ash aggregate (SFA) is one of the most commonly used lightweight aggregates produced from an industrial waste called fly ash [6,7]. LWAC made with SFA is sustainable, eco-friendly, possesses good mechanical performance, and is economical and durable for structural applications [8]. Microstructural studies have shown that the interfacial transition zone (ITZ) of lightweight concrete made with SFA is denser than conventional concrete made with natural coarse aggregate (NCA). Due to this, a better bond exists between SFA and cement paste in LWAC [9].

Despite the advantages of LWAC, its usage in the construction of load-bearing elements is not widely considered due to little understanding of its engineering properties. The primary reason for the low acceptance of lightweight concrete for structural elements is its brittleness. For the same mix proportions and compressive strength, the brittleness of lightweight concrete is higher than that of conventional concrete [10]. The increased brittleness in LWAC is due to crack propagation directly through the lightweight aggregate [11]. However, it is possible to resolve the drawback by including fibres in concrete and thus increasing its ductility. The use of synthetic fibre is very convenient in lightweight concrete due to its low specific gravity and ease of handling

* Corresponding author.
E-mail address: suriyap@ce.iith.ac.in (S. Suriya Prakash).

https://doi.org/10.1016/j.istruc.2023.02.099
Received 4 November 2022; Received in revised form 4 February 2023; Accepted 20 February 2023
Available online 28 February 2023

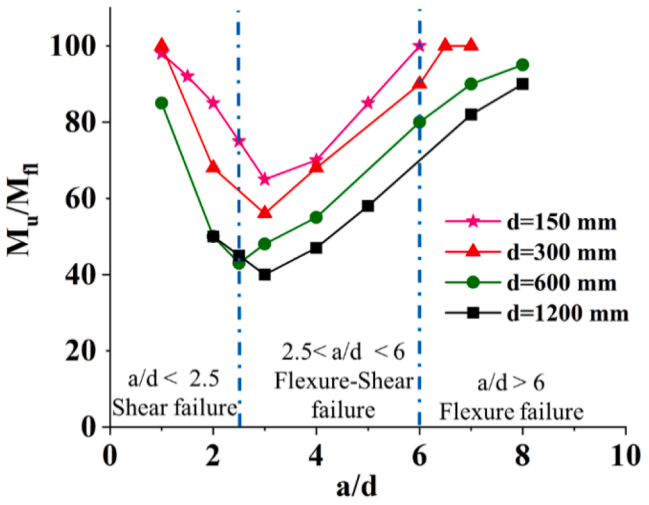

Fig. 1. Effect of a/d ratio on the behaviour of reinforced concrete beams [33].

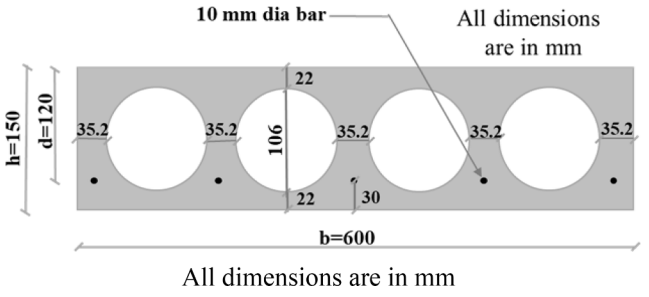

Fig. 2. Cross section of HCS.

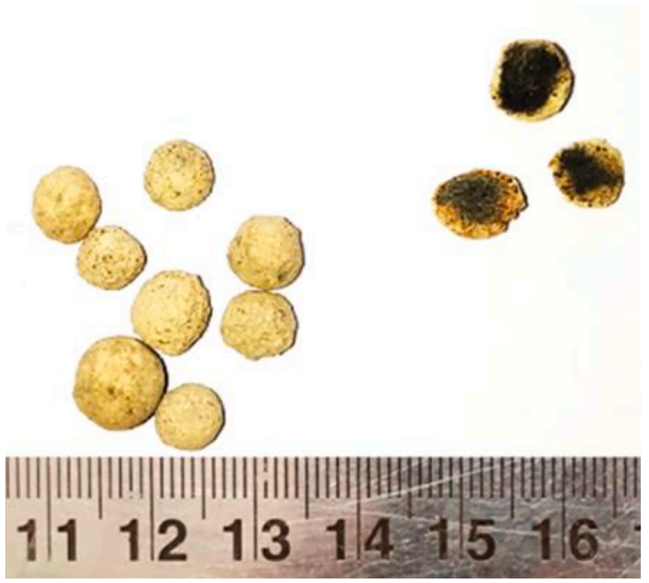

Fig. 3. SFA.

[12]. Furthermore, synthetic fibres show good corrosion resistance, excellent post-cracking behaviour, chemical stability and have a lesser adverse impact on workability [13,14]. The synergistic action between macro and micro synthetic fibres enhances the performance of concrete by arresting crack propagation at different scales [11]. Moreover, adding different combinations of steel and synthetic fibres causes a longer crack propagation time, higher ultimate failure loads, and improved stiffness in HCS [15].

Numerous researchers in the past have examined the flexural behaviour of HCS made of normal-density concrete [16–19]. Naser et al. [20] studied the flexural behaviour of steel fibre-reinforced ferrocement HCS with embedded polyvinyl chloride (PVC) pipe. The researchers reported an increase in the ductility and serviceability of HCS compared to solid slabs [2]. Earlier researchers have explored the behaviour of HCS under shear [21–24]. Several researchers also studied the shear behaviour of fibre-reinforced hollow core slab (FR-HCS) and concluded that adding fibres helps to increase the shear capacity, ductility and delays the crack propagation [23,25,26]. The shear strength of HCS is primarily influenced by concrete strength, loading conditions, and interlocking forces in the crack path [26]. Previous studies have shown that the hollow-core slabs tested at shear span to depth ratio (a/d) less than 3.5 usually fail in web shear failure mode [22]. According to researchers, many design codes do not adequately predict the shear capacities of hollow core slabs [27,28]. All the shear capacity equations were derived assuming the equivalent rectangular section or I-section of the hollow core section. However, the stresses generated at the voids of HCS may lead to reduced shear strength [22]. Various reinforced concrete (RC) elements have shown enhanced shear strength due to macro synthetic fibre addition [29–31]. Previous works have shown that synthetic fibres could increase the strength of HCS [32]. However, the extent of performance improvement of hollow core slabs due to the addition of macro synthetic is not established yet.

Kani's [33] classical theory states that a/d ratio of 6 is the transition value and the RC beams tested at a/d greater than 6 usually fail in flexural mode (Fig. 1). For a/d ratios between 2.5 and 6, RC beams typically fail due to sudden diagonal shear stress followed by flexural cracking (flexure-shear mode). Specimens with an a/d ratio less than 2.5 fail in shear critical mode. However, the previously established a/d ratio ranges are only valid for RC beams and not for HCS and LWHCS. Numerous researchers have used the finite element method in the numerical analysis of the shear behaviour of HCS [21,34–36]. Several researchers have examined the application of the finite element method to lightweight concrete and synthetic fibre-reinforced concrete (FRC) separately using ABAQUS [37–40].

2. Research significance

A critical review of earlier studies shows that several studies have been carried out on varying shear span to depth ratios of HCS specimens made of conventional concrete. On the contrary, the studies on structural behaviour of light weight concrete are very limited. Moreover, previous studies have not focused on the behaviour of fibre reinforced lightweight hollow core slabs (FR-LWHCS) at different flexure-to-shear ratios. Hence, this study aims at the experimental and numerical investigation of FR-LWHCS at different a/d ratios. The specific objectives of the study are-.

- To understand the ultimate strength, serviceability performance, failure modes, and toughness of FR-LWHCS through full-scale testing at various a/d ratios of 3.5, 7, and 10.
- To understand the influence of synthetic fibres on the response of lightweight HCS in terms of crack propagation and post-cracking behaviour based on full-field strain measurements using the DIC technique at different a/d ratios.
- To carry out finite element analysis on the response of FR-LWHCS at different a/d ratios of 3.5, 7 and 10 to understand the crack patterns and failure modes.

3. Experimental program

The experimental program involved construction and testing of total 12 HCS specimens with normal and lightweight concrete at a/d ratios of 3.5,7 and 10. All the HCS specimens were of the dimensions 3400 mm

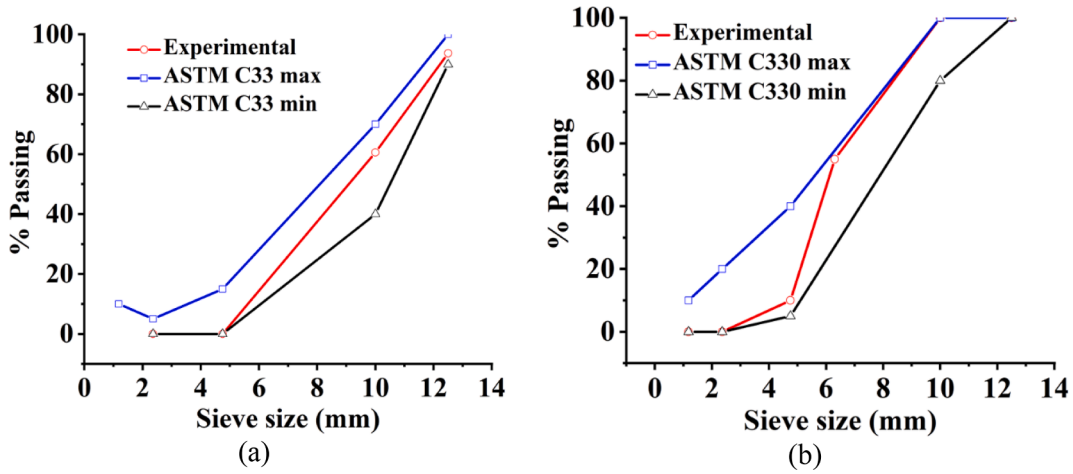

Fig. 4. Gradation of coarse aggregates: (a) 10 mm aggregate (b) SFA.

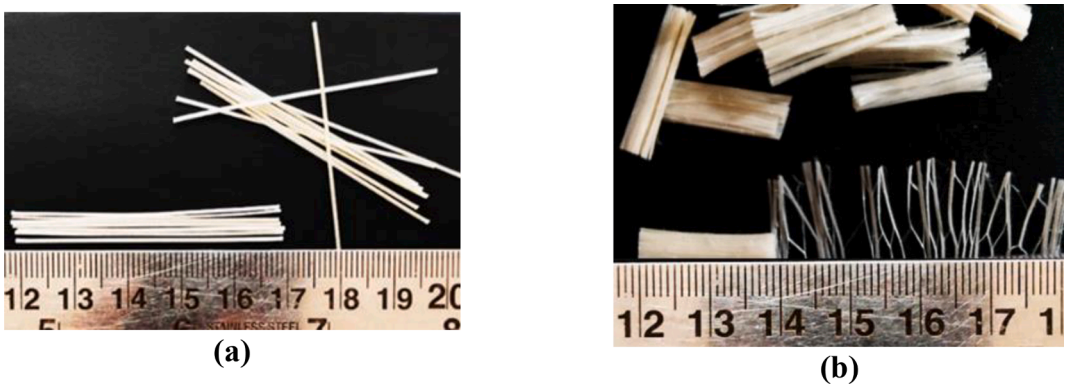

Fig. 5. Fibres: (a) Macro synthetic **(b)** Micro synthetic.

Table 1
Properties of fibres and reinforcement.

Parameters	Shape	Diameter (mm)	Specific Gravity	Length (mm)	Elastic Modulus (GPa)	Tensile Strength (MPa)
Macro fibre	Structural fibre	0.50	0.91	50	10.0	618
Micro fibre	Fibrillated fibre	0.08	0.91	19	4.9	400
Steel rebar	–	10.00	7.80	3400	196.0	550

Table 2
Optimized concrete mix proportions.

Specimen	NCA	PO00	PO04	PO06
Cement (kg/m^3)	350	350	350	350
Fly ash (kg/m^3)	35	35	35	35
Sand (kg/m^3)	520	520	520	520
Sintered fly ash aggregate (kg/m^3)	0	800	800	800
Natural coarse aggregate (kg/m^3)	1450	0	0	0
Water (kg/m^3)	115	115	115	115
Water /Binder ratio	0.30	0.30	0.30	0.30
Superplasticizer (kg/m^3)	0.3	0.3	0.8	1.0
Macro fibres (kg/m^3)	0	0	3.68	5.52
Micro fibres (kg/m^3)	0	0	0.184	0.184

Table 3
Summary of material properties.

Parameters	NCA	PO00	PO04	PO06
Compressive strength of concrete cubes (in MPa)	45 (0.5)	40 (1.5)	42 (1.5)	46 (1)
Tensile Strength (from inverse analysis) (in MPa)	2.4	2.2	2.25	2.4
Split tensile strength of cylinders (in MPa)	3.8 (0.2)	2.9 (0.1)	3.5 (0.1)	4.3 (0.2)

*Values in parenthesis are standard deviation (MPa) of measured strength.

length, 600 mm width, and 150 mm thickness. Each HCS specimen contains four circular voids of 106 mm diameter each. Five steel rebars were placed at an effective cover of 30 mm in the tension zone. The specimens were manufactured and tested at Structural Engineering Laboratory, IIT Hyderabad. The cross-sectional view of the HCS is shown in Fig. 2.

3.1. Material properties

Ordinary Portland Cement (OPC-53 grade), fly ash (class F), SFA, natural coarse aggregate (NCA), natural sand, synthetic fibres, potable

Table 4
Details of the specimens tested.

Specimen ID	Type of concrete	Fibre dosage (%)	Shear span to depth (a/d) ratio
NCA-HCS-3.5	Conventional concrete with natural coarse aggregate (NCA)	0	3.5
NCA-HCS-7		0	7
NCA-HCS-10		0	10
PO00-HCS-3.5	Lightweight concrete reinforced with polyolefin (PO) fibres	0	3.5
PO00-HCS-7		0	7
PO00-HCS-10		0	10
PO04-HCS-3.5		0.4	3.5
PO04-HCS-7		0.4	7
PO04-HCS-10		0.4	10
PO06-HCS-3.5		0.6	3.5
PO06-HCS-7		0.6	7
PO06-HCS-10		0.6	10

water, and superplasticizer were used to prepare normal and lightweight concrete. The specific gravity of cement, fly ash, SFA, NCA, and natural sand used is 3.15, 2.2, 1.45, 2.6 and 2.6, respectively. The SFA (Fig. 3) used in this study range in size from 4 to 8 mm and has a water absorption rate of 15 %. The study used NCA with a maximum size of 10 mm and water absorption of 0.8 %. The particle size distributions for NCA and SFA are shown in Fig. 4 (a) and Fig. 4 (b), and they meet the ASTM C330 [41] and ASTM C33 [42] limits, respectively. Natural river sand having a water absorption of 3 % is taken as fine aggregate. The superplasticizer used in the study was a high-range polycarboxylate ether-based water reducer. Two polyolefin-based macro and micro synthetic fibres were used in the construction of FR-LWHCS. Fibres used are shown in Fig. 5, and their properties are listed in Table 1. The macro-fibre dosages of 0.4 % and 0.6 % with a constant micro-fibre dosage of 0.02 % were added. Micro-fibres are generally added to reduce the shrinkage cracking. Typically, manufacturers recommend about 0.02 % – 0.09 % fibre dosage by volume of concrete. However, a lower dosage (0.02 %) of micro fibres was considered in the study due to its hybrid blending with macro fibres for optimizing the cost. it is seen that a fixed dosage of 0.02 % along with macro fibres is shown to produce good results[43]. Steel rebars (10 mm dia.) were used as primary reinforcement in the construction of all the HCS.

3.2. Mix design and specimen details

The mix design used in the manufacturing of LWHCS is based on the previous work of authors [8]. An optimized concrete mix design for 1800 kg/m^3 density was obtained using volumetric mix proportions to achieve a minimum compressive strength of 40 MPa. HCS specimens without fibres are designated as control specimens (PO00-HCS). HCS specimens reinforced with fibres are referred to as PO04 and PO06. In the nomenclature, PO, 04, 06 denotes polyolefin fibres, 0.4 % and 0.6 % of the volume of fibre dosage, respectively. A HCS of normal density was also cast with NCA and labelled as NCA-HCS which serves as a reference for comparison of the structural behaviour. Additionally, three concrete cubes of size 150 mm × 150 mm × 150 mm were cast for each mix to study the compressive strengths. The 28-day average compressive strengths of mixes PO00, PO04, PO06, and NCA were 40 MPa, 42 MPa,

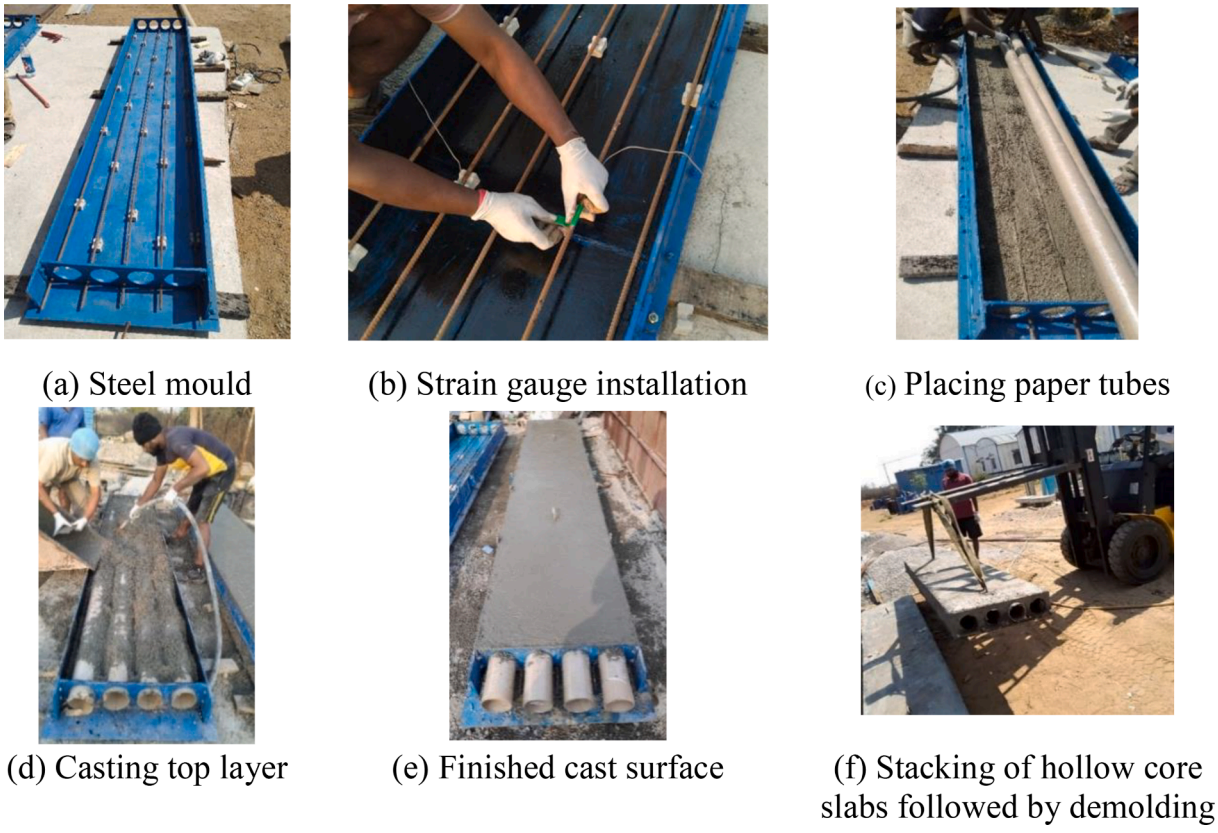

Fig. 6. Casting of Lightweight HCS.

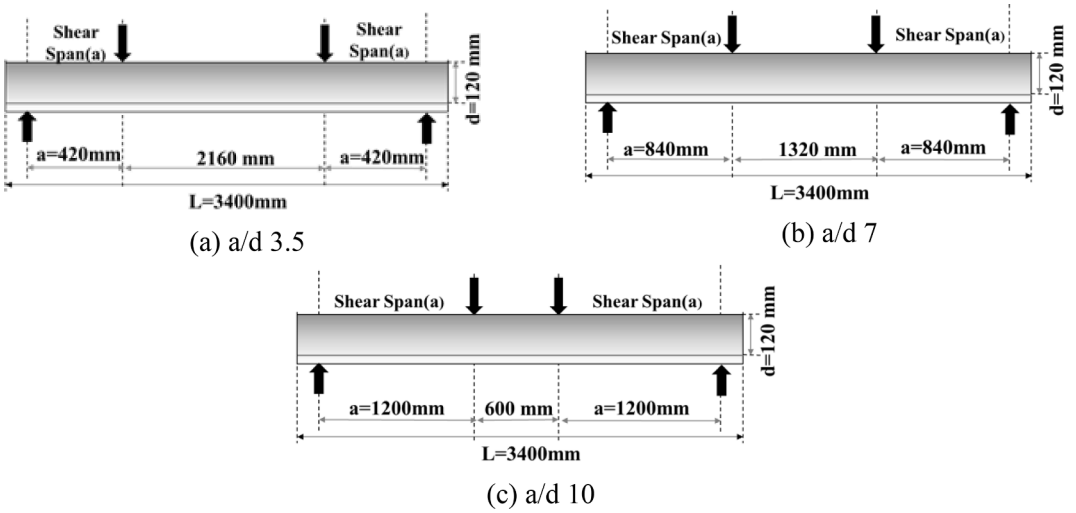

Fig. 7. Loading configuration for all a/d ratios.

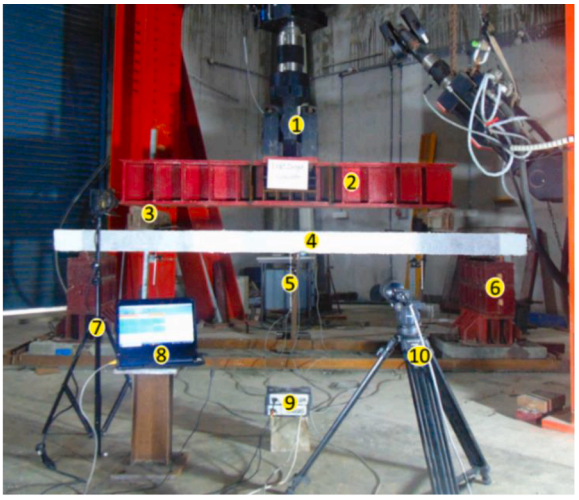

Note: 1-MTS Actuator, 2-Steel Spreader Beam, 3-Loading I-Beam, 4- Hollow Core Slab, 5-LVDT, 6- Support Beam, 7- Light Source, 8-Monitor, 9- DAQ, 10- DIC Camera

Fig. 8. Experimental test setup.

46 MPa, and 45 MPa. The optimised concrete mix design is shown in Table 2. The detailed discussion on the mechanical characterization of synthetic fibre-reinforced SLWAC for mix design, stress–strain behaviour under compression, fracture behaviour, and splitting tensile properties can be found elsewhere [8,11]. The summary of material properties is given in Table 3. The specimen details are given in Table 4.

3.3. Mould preparation and casting

Special moulds presented in Fig. 6(a) were used for construction of HCS. The rebars and the paper tubes were inserted through the slots provided in the mould. The two rebars adjacent to the centre rebar were instrumented with two strain gauges at mid-length. The moulds were cleaned and oiled to avoid adhesion to the concrete. Initially, cement, sand, and SFA were dry-mixed for 2 min in a tilted drum mixer to attain a homogeneous mix. Following this, 50 % of the total water was added and mixed for two to three minutes. Subsequently, the remaining 50 % of the water was added with a superplasticizer and mixed for another 3 to 5 min. Later, the fibres were added to the mix. After thoroughly mixing, the concrete was poured into the moulds. The bottom flange was cast first. Following that, the paper tubes were inserted into the holes after being thoroughly wrapped in a wrapping film. The top flange was then cast, followed by extensive vibration. The specimens were demoulded after 24 h, water-cured for 28 days, and stacked in a queue for testing. The whole process of construction is shown in Fig. 6.

3.4. Test Set-up and instrumentation

The HCS specimens were tested under a displacement-controlled four-point bending using a hydraulic actuator of 1000 kN capacity. The shear span to depth (a/d) ratios considered were 3.5, 7 and 10 (Fig. 7). The surface of the HCS was prepared and levelled using high-strength cement mortar over which the loading I-beams were placed. The load was applied to the specimen as distributed line loads using two transverse I-beams attached to a rigid steel spreader beam, as shown in Fig. 8. Load was increased monotonically in displacement control mode at a constant rate of 0.03 mm/s. A linear variable displacement transducer (LVDT) with a stroke of 200 mm was placed at its mid-span to

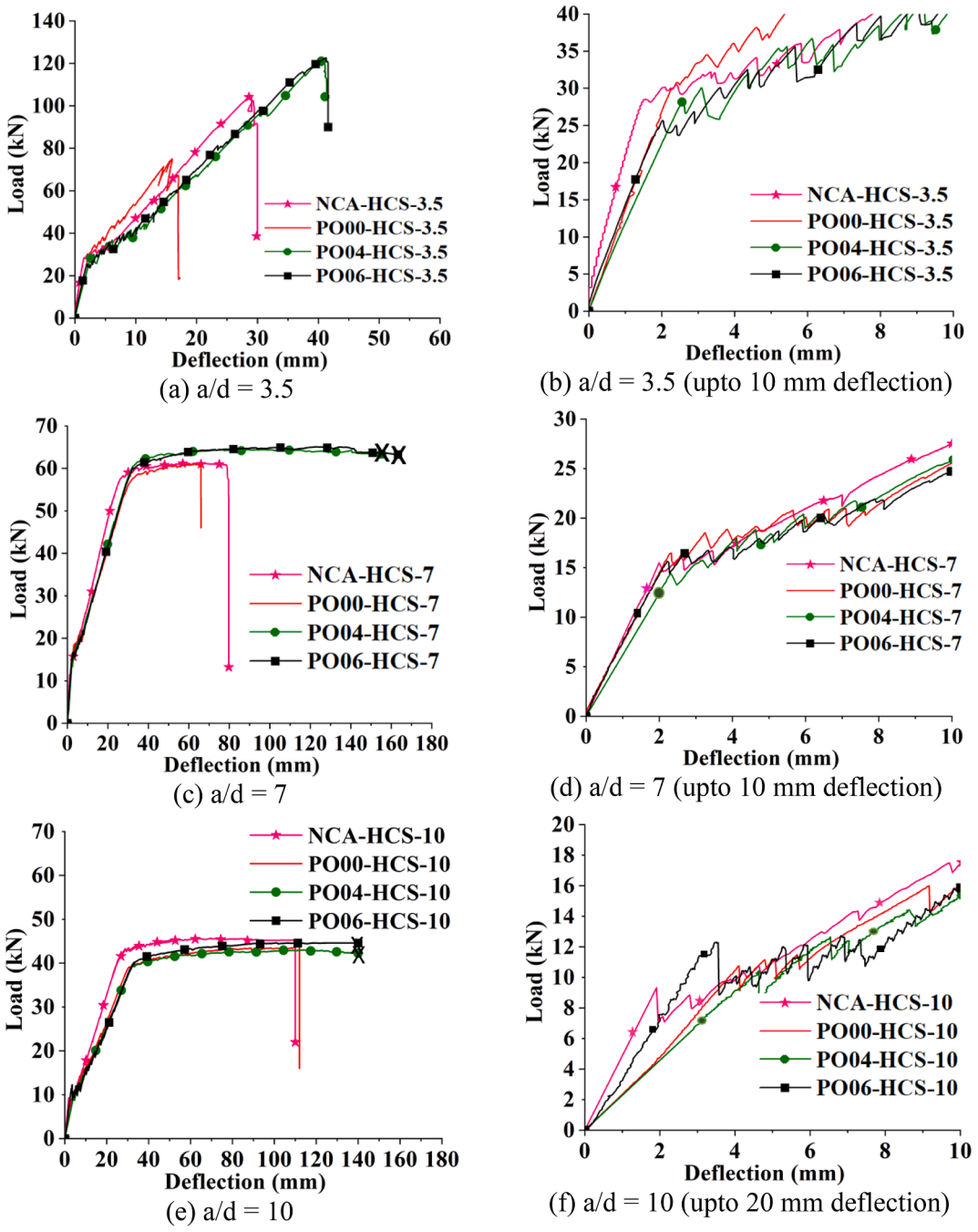

Fig. 9. Load vs Deflection curve.

track the mid-span deflection of the HCS specimen. Additionally, the strain in steel rebars was recorded using the strain gauges attached to the rebars during the construction of the specimen. On the soffit of the HCS, two LVDTs of 50 mm capacity were mounted to measure deflections at the loading points. The applied load was measured automatically with the load cell of the actuator. All sensors were connected to the data acquisition system (DAQ) for continuous data collection during testing. All the specimens were tested within 28 to 32 days after construction to ensure the uniform compressive strength of concrete at the time of testing.

4. Experimental results and discussion

4.1. Load vs deflection behaviour

The load vs mid span deflection curves of the tested HCS are shown in Fig. 9. The response of the specimens presented ascertain the understanding that the NCA concrete possess higher pre-cracking stiffness. Additionally, the addition of fibres does not significantly influence the cracking load of the HCS tested at a particular a/d ratio (Table 5).

The load vs deflection curve for HCS specimens at a/d ratio 3.5 is presented in Fig. 9 **(a)**. The behaviour exhibited by the specimen can be divided into three stages (i) pre-cracking stage (ii) post-cracking stage,

Table 5
Summary of experimental results.

Specimen	a/d	CL(kN)	Δ_{CL}(mm)	PL(kN)	Δ_{PL}(mm)	$L\Delta_{mmax}$(mm)	Δ_{mmax}(mm)	M_{CR}(kN-m)	M_P(kN-m)	EA(Joule)	Mode of failure**
NCA-HCS-3.5	3.5	28.4	1.5	102.5	29.3	84.0	30.0	6.0	21.5	1880	S
PO00-HCS-3.5	3.5	30.7	2.4	75.0	16	67.3	16.9	6.4	15.7	816	S
PO04-HCS-3.5	3.5	28.5	2.6	121.4	40.4	121	40.4	6.0	25.5	2871	S
PO06-HCS-3.5	3.5	25.6	2.0	122.6	41.2	122.6	41.2	5.4	25.7	2977	S
NCA-HCS-7	7	15.5	2.0	61.2	57.1	53	79.7	6.5	25.7	4130	F-S
PO00-HCS-7	7	16.4	2.3	60.9	62.5	60.4	65.9	6.9	25.6	3148	F-S
PO04-HCS-7	7	14.4	2.3	64.4	96.0	63.3	155.3*	6.0	27.0	8019*	F-S
PO06-HCS-7	7	15.6	2.2	65.1	123.0	63.2	163.0*	6.5	27.3	7978*	F-S
NCA-HCS-10	10	9.3	1.9	45.6	70.0	45.2	110.0	5.6	27.3	4535	F
PO00-HCS-10	10	10.7	4.1	43.9	110.0	43.8	112.0	6.4	26.3	4105	F
PO04-HCS-10	10	10.4	4.6	43.0	114.0	42.2	140.0*	6.2	25.8	5233*	F
PO06-HCS-10	10	12.2	3.5	44.6	101.0	44.5	140.0*	7.3	26.7	5404*	F

* = testing has been stopped before failure.
** Mode of failure, CL – Cracking load, Δ_{CL}- Deflection at cracking load, PL – Peak load, Δ_{PL}- Deflection at peak load, L Δ_{mmax}- Load at measured maximum deflection, Δ_{mmax}- Measured maximum deflection, M_{CR}- Cracking moment, M_P- Peak moment, EA- Energy absorption capacity, S: Shear, F-S: Flexural-shear, F: Flexure.

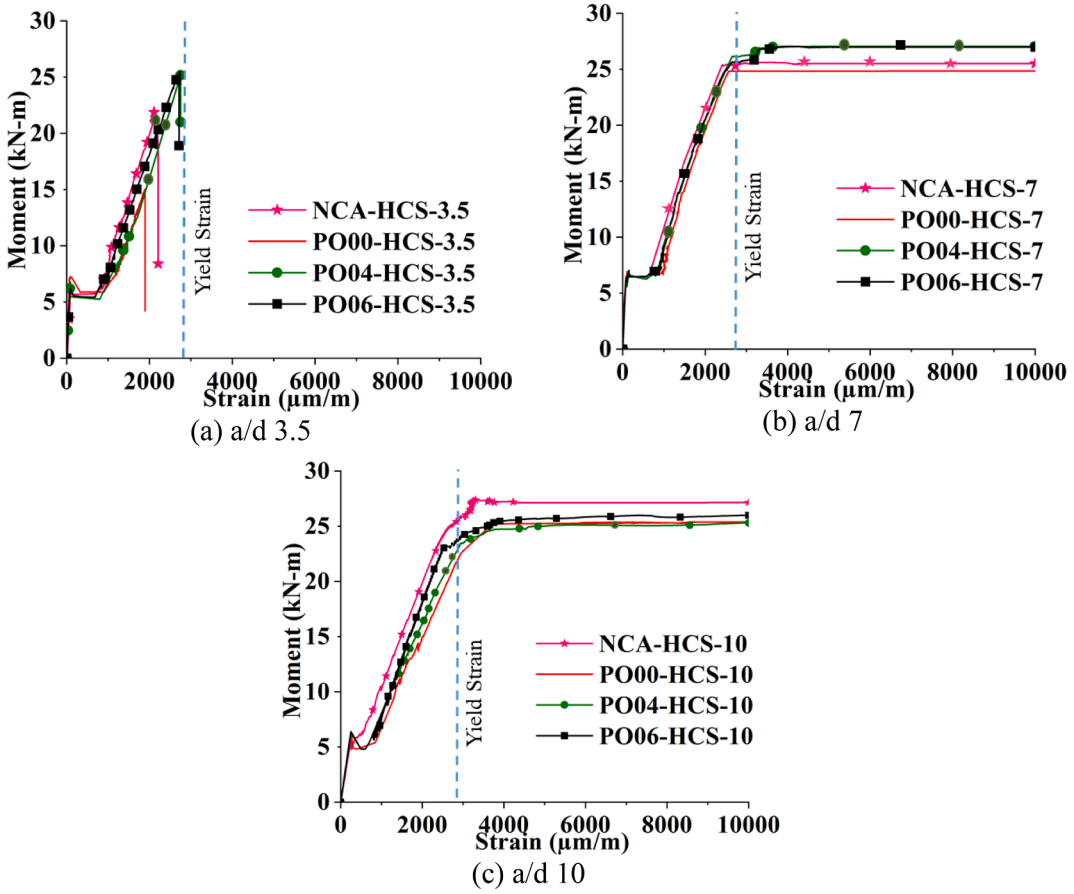

Fig. 10. Moment vs strain behaviour of rebar.

and (iii) failure stage. In pre cracking stage, the behaviour of the curve is elastic and the load increases proportionally with the increase in deflection. After the cracking of concrete, the stiffness can be observed to decrease. However, the load increases linearly with the deflection until it reaches the peak load. After reaching the peak, the specimens have no residual strength, the load drops abruptly, and the collapse is observed to be brittle. All the specimens tested at a/d of 3.5 exhibited similar pre-cracking behaviour with cracking load in the vicinity of 25 kN (Fig. 9 **(b)**). Addition of fibres enhanced the load carrying capacity of the members when compared to the control specimens which do not have any fibres. However, no significant increase was observed when the fibre dosage was increased from 0.4 % to 0.6 %. The increased load carrying capacity of the HCS reinforced with fibres resulted in higher energy absorption capacity, yet the members failed in a brittle manner.

The load vs deflection response of the hollow core slabs evaluated at a/d ratio 7.0 is shown in Fig. 9 **(c)**. The behaviour of the curve is also divided into three stages (i) pre-cracking stage, (ii) post-cracking stage, and (iii) post-yielding of the longitudinal bar. In the pre-cracking stage, the load resistance increases linearly with applied displacement until the concrete on the tension face of the slab cracks. The second stage of the

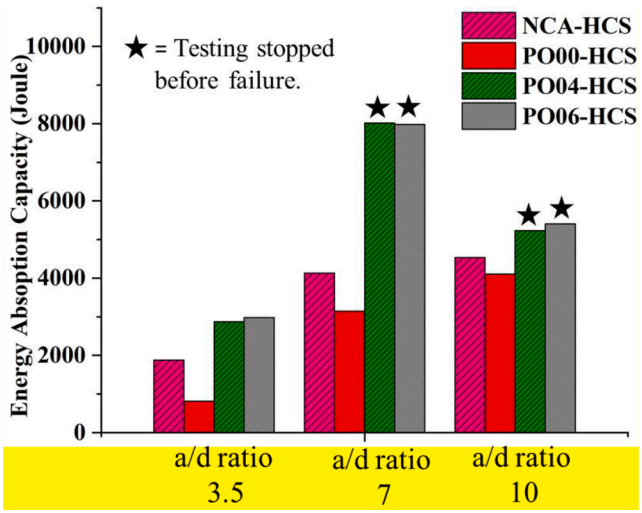

Fig. 11. Energy absorption capacities at different a/d ratio.

curve begins after flexural cracking with a reduced stiffness and extends until longitudinal rebar yields. The third stage starts with the rebar yielding to the specimen's failure. As the specimens were tested at a/d of 7.0, the specimen is subjected to higher bending moments, thus increasing the axial strains in the rebar. Increase in the applied displacements lead to the yielding of steel and thus capping the moment carrying capacity of the member. The comparison of response of all the specimens tested at a/d ratio of 7 is shown in Fig. 9 **(c)**, and it can be observed that all the specimens showed similar trend. Addition of fibres enhanced the deflection at maximum load and energy absorption capacity. However, the peak load increased marginally with the addition of fibres. The pre-cracking and post-cracking stiffness of normal density concrete (NCA-HCS-7) was higher than the lightweight concrete counter parts (Fig. 9 **(c)**). The zoomed-in portion up to 10 mm is shown in Fig. 9 **(d)**. All the test findings such as cracking load, peak load, maximum measured load and their corresponding deflection are shown in Table 5. The table also summarises the cracking moment, peak moment, and energy absorption capacity.

Fig. 9 **(e)** depicts the load vs deflection curve of hollow core slabs assessed at a/d ratio 10. The behaviour of the graph is exactly similar to the a/d ratio 7. It is seen that the inclusion of fibres does not considerably increase peak load but does improve deflection at maximum load and energy absorption capacity. The zoomed-in portion up to 10 mm is shown in Fig. 9 **(f)**. The area under the load–deflection curve was used to compute the energy absorption capacity of all HCS specimens. For all a/d ratios, it is concluded that the energy absorption capacity of PO06-HCS was the highest, followed by PO04-HCS, NCA-HCS and PO00-HCS.

4.2. Moment at mid span vs strain behaviour

Strain gauges mounted on the rebars at mid-length of HCS to monitor strain variations during testing. Strain values up to 10,000 μm/m were measured. The variation of strain in the rebar corresponding to the moment at mid span is presented in Fig. 10. It should be noted that the strains in the rebars were insignificant until the specimen cracked. The strains increased significantly after cracking, as predicted. The specimens tested at a/d ratio 3.5 initially cracked in shear. The slope of the curve showed a reduction after the initial crack as shown in Fig. 10(a). The specimens failed before the yielding of steel rebar and thus the strain variation doesn't show any yield plateau.

The initial crack in the specimen tested at a/d ratios 7 and 10 was due to the formation of a flexure crack. The strain corresponding to a moment is lower in the fibre-reinforced HCS specimens (PO06-HCS and PO04-HCS) than in the control specimen (PO00-HCS), demonstrating the role of fibres in load resistance. However, under a given moment, the strain of the NCA-HCS specimen is marginally higher than other specimens. Steel rebar yielded before reaching the maximum moment in all HCS specimens tested at a/d ratio of 7 and 10. The addition of fibres resulted in an increase in the moment capacity of HCS specimens tested at a/d of 3.5. However, the specimens showed a shear-dominant failure.

4.3. Energy absorption capacity

Energy absorption capacity is one of the essential criteria in determining the efficiency of various fibres and their dosage for specific applications. The area under the load–deflection curve is considered to evaluate the energy absorption capacity. The deflection up to failure or 140 mm, whichever is less, is used to calculate the energy absorption capacity. The addition of fibres leads to the gradual propagation of cracks through bridging action thus delaying the failure. Hence, fibre-reinforced specimens have a high energy absorption capacity. The energy absorption of all specimens tested at different a/d ratios is depicted in Fig. 11. The energy absorption capacity of the specimens that failed in flexure (a/d = 10) and flexural-shear (a/d = 7) is higher than that of specimens that failed in shear (a/d = 3.5) due to well-distributed cracks in flexure and flexural-shear failure. The addition of fibres led to an increase in the energy absorption capacity of members tested at a particular shear span. Thus, showcasing the positive effect of fibre addition.

4.4. Crack distribution and failure modes

The failure modes and crack distribution of all the specimens are represented in Fig. 12. The HCS specimens tested with an a/d ratio of 3.5 failed in shear. Initially, a minor shear crack developed in the tension zone at the shear span region when the specimen cracked. As the load increases, the crack propagates towards the loading point. The failure was sudden and brittle in control HCS specimens. In the specimens reinforced with fibres, the number of diagonal shear cracks increased. There was a sign of failure in fibre reinforced HCS specimens before the specimens failed in diagonal shear tension of failure of concrete.

The HCS specimens tested at an a/d ratio of 7 failed in flexural-shear failure mode. Initially, when the specimens reached the cracking load, a flexure crack formed at the constant moment zone at the tension surface of HCS specimens. As the load increased, several flexural cracks occurred at the constant moment zone, and a few shear cracks occurred at the shear span zone. Later, the cracks began to widen and propagate towards the compression surface. The number of cracks in PO00-HCS was lesser than that of NCA-HCS. The crack in lightweight concrete (POO-HCS) passes through the aggregate, whereas the crack in normal density concrete (NCA-HCS) passes around the aggregate. Hence, the PO00-HCS specimen failed earlier than the NCA-HCS specimen. The number of cracks was substantially higher in fibre reinforced HCS specimens than in control HCS specimens. In fibre-reinforced specimens, cracks were more evenly distributed, and the space between cracks was shorter. The specimens tested in the a/d ratio of 7 and 10 were more ductile due to rebar yielding than those tested in the a.d ratio of 3.5.

HCS specimens tested at a/d ratios of 10 failed in flexural mode. When the specimens cracked, a flexure crack started at the bottom face of the tension zone. Upon increasing the loads, several flexure cracks formed at a constant moment and propagated towards the compression face of the slab. Cracks were more in number in fibre-reinforced specimens compared with control specimens. In fibre-reinforced specimens, the distance between the cracks was lesser than in control specimens. In addition, the cracks were distributed and branched in fibre-reinforced specimens.

4.5. DIC analysis

Digital image correlation (DIC) is a technique for measuring full-field

(a) NCA-HCS- a/d 3.5

(b) PO00-HCS- a/d 3.5

(c) PO04-HCS- a/d 3.5

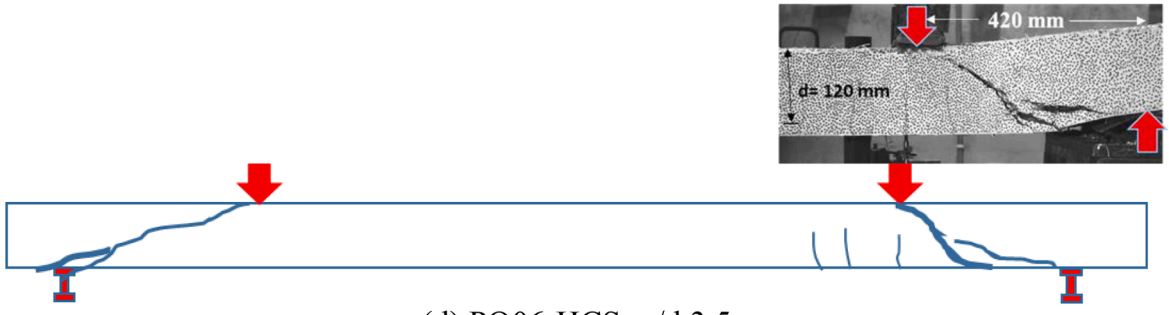

(d) PO06-HCS- a/d 3.5

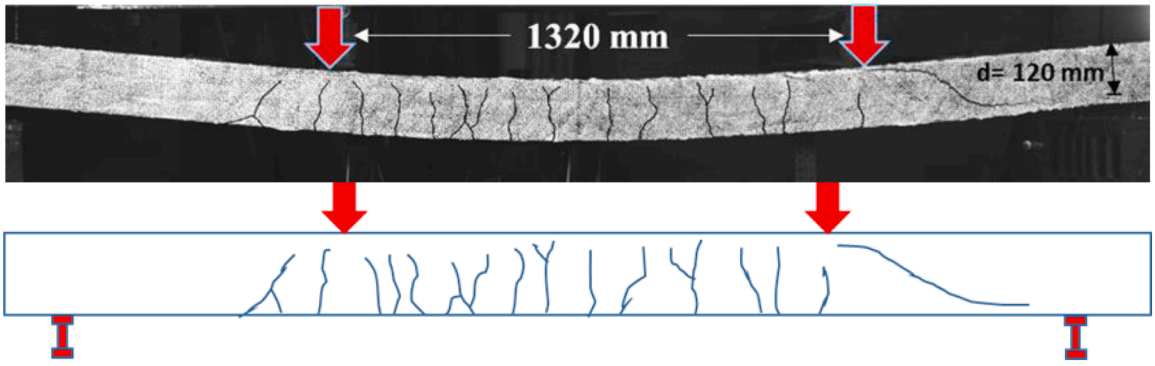

(e) NCA-HCS- a/d 7

Fig. 12. Failure modes and crack distribution.

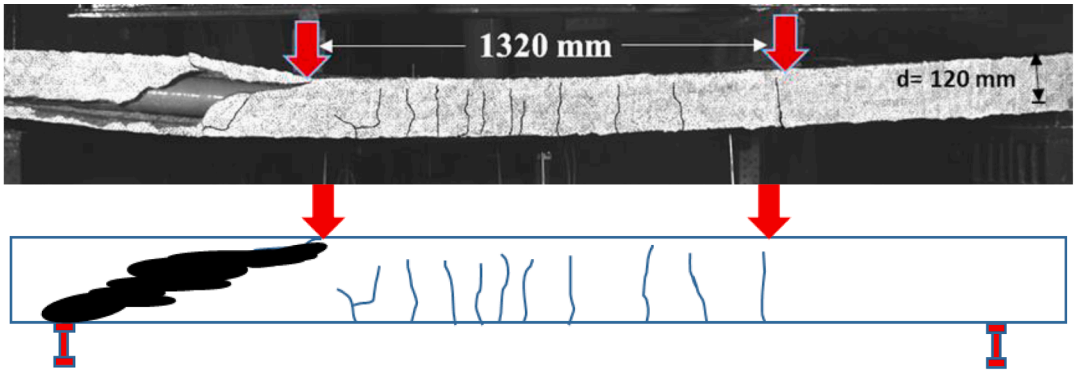

(f) PO00-HCS- a/d 7

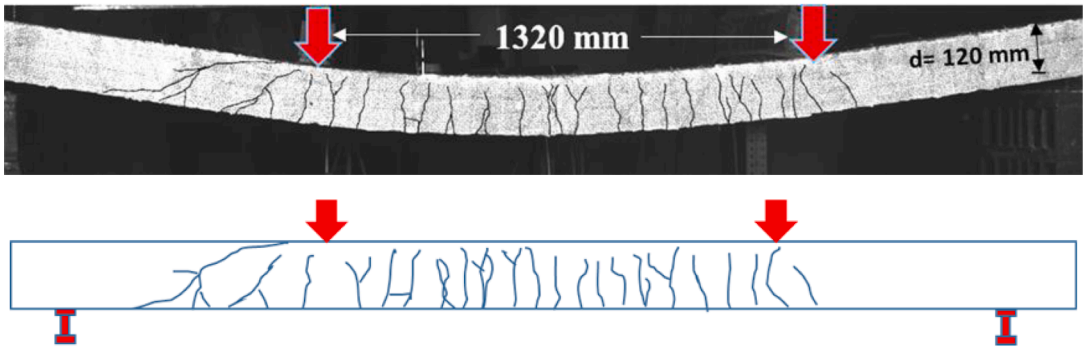

(g) PO04-HCS- a/d 7

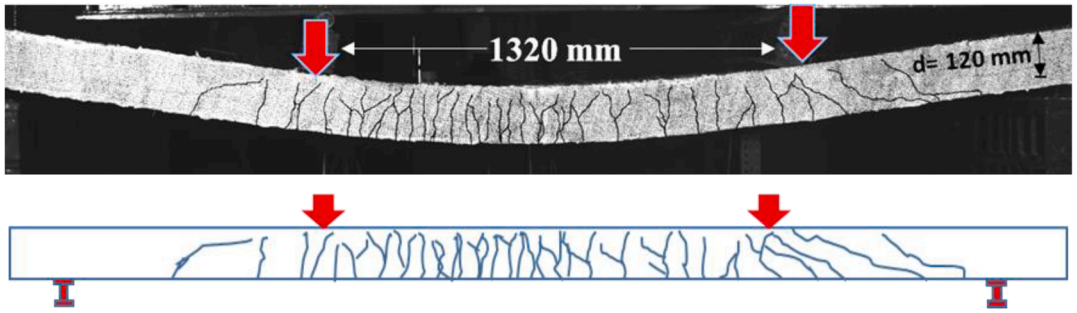

(h) PO06-HCS- a/d 7

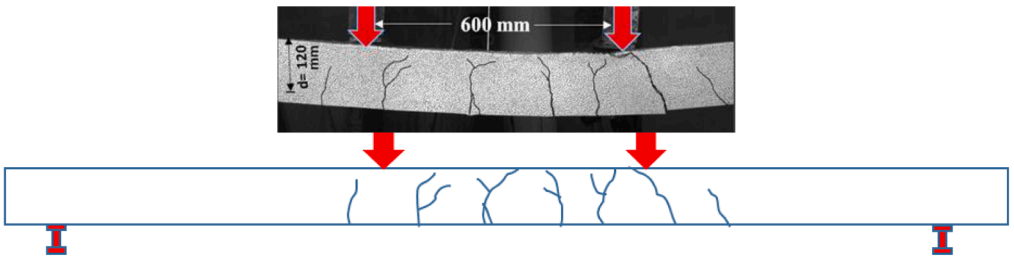

(i) NCA-HCS- a/d 10

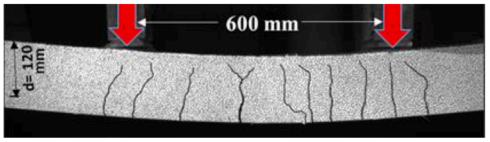

Fig. 12. (*continued*).

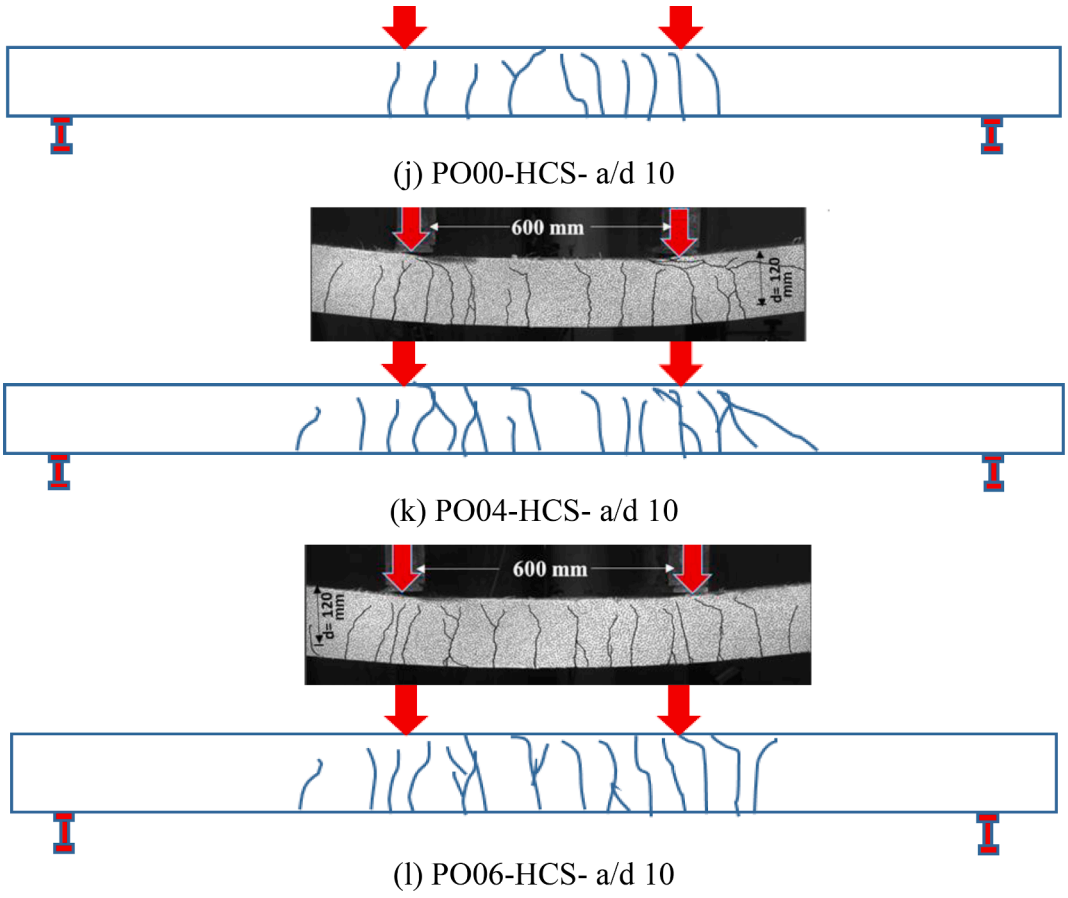

Fig. 12. (*continued*).

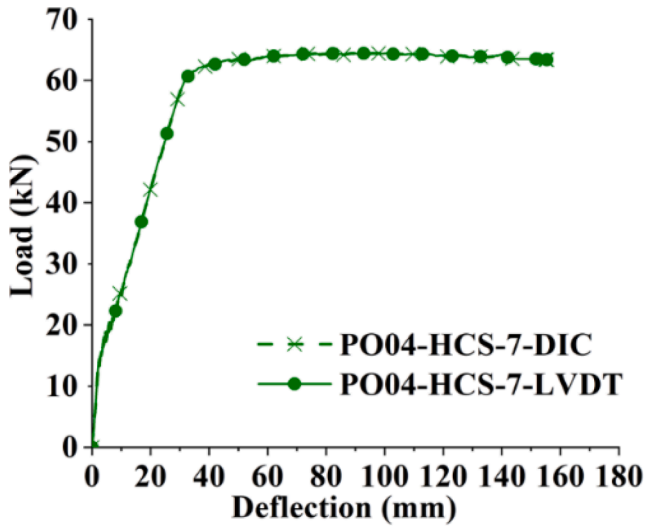

Fig. 13. Load vs Deflection comparison between LVDT and DIC results.

strain and localised displacements in the HCS specimen by correlating the speckled patterns on images captured at different intervals during testing [44]. DIC analysis can predict the structural behaviour of concrete successfully when used in conjunction with conventional measurements and after proper calibration [31,45,46]. The whole process can be classified into three phases. The first phases included the preparation of specimens and image capturing. During the second phase, the images were analysed by correlating the captured images with the help of vic-2D 2009 [47] software. The last phase is post-processing, where the data are extracted from the analysed images [48]. The surface of the HCS specimen was painted with acrylic-based white paint, followed by random speckling using a black marker. In this study, a camera with a resolution of 1024x768 was used, which captured images with a frequency of 2 Hz. To process the images optimally, a calibration image (with scale) and a reference image (with the unreformed shape) were captured before applying the load. DIC works on the principle of pattern matching, which correlates the speckle patterns in the un-deformed and deformed images to determine corresponding strain and displacement.

The accuracy of the DIC results depends on the size of the speckles and the subset chosen for analysis. The subset and step size were decided based on previous literature [49]. A crack propagating through a specimen during the test may result in a loss of correlation in the area surrounding the crack. The loss of correlation near a crack permits the identification of a physical opening which is reflected in the digital data. The load–deflection behaviour of the twelve HCS specimens was compared using DIC analysis and LVDT (at mid-span) measurements. As demonstrated in Fig. 13, the DIC analysis results agreed with the test results measured with LVDT. To maintain brevity, the validation of the load–deflection behaviour of only one specimen (PO04-HCS) tested at a/d ratio 7 is presented. Table 6a and 6b shows a comparison of displacement measured by LVDT and DIC at various load points (at cracking, at peak, and at ultimate). Due to the initial slack in the LVDTs, the cracking deflection from experiments is found to be different from the results from DIC. However, at larger deflections, the absolute error (E_{abs}) in displacement measured by LVDT and DIC is found to be marginal.

4.5.1. *Strain contours*

The crack initiation, propagation and growth are analysed with the

Table 6a
Comparison of displacement between LVDT and DIC measurements at different load points.

Specimens	Cracking load			Peak load			Ultimate Load		
	Δ_{EXP} (mm)	Δ_{DIC} (mm)	E_{abs} (mm)	Δ_{EXP} (mm)	Δ_{DIC} (mm)	E_{abs} (mm)	Δ_{EXP} (mm)	Δ_{DIC} (mm)	E_{abs} (mm)
NCA-HCS-3.5	1.5	1.6	0.1	29.3	29.4	0.1	30.0	30.1	0.1
PO00-HCS-3.5	2.4	2.4	0	16.0	16.1	0.1	16.9	17.0	0.1
PO04-HCS-3.5	2.6	2.4	0.2	40.4	40.7	0.3	40.4	40.7	0.3
PO06-HCS-3.5	2.0	2.1	0.1	41.2	41.3	0.1	41.2	41.3	0.1
NCA-HCS-7	2.0	2.14	0.14	57.1	57.2	0.1	79.7	79.9	0.2
PO00-HCS-7	2.3	2.33	0.03	62.5	61.9	0.6	65.9	65.0	0.9
PO04-HCS-7	2.30	2.31	0.01	96.0	96.1	0.1	155.3*	155.3*	0.3
PO06-HCS-7	2.2	2.2	0	123.0	123.7	0.7	163.0*	163.8*	0.8
NCA-HCS-10	1.9	1.9	0	70.0	70.1	0.1	110.0	110.2	0.2
PO00-HCS-10	4.1	4.6	0.5	110.0	110.6	0.6	112.0	112.6	0.6
PO04-HCS-10	4.6	5.2	0.6	114.0	114.8	0.8	140.0*	140.8*	0.8
PO06-HCS-10	3.5	3.0	0.5	101.0	105.0	4.0	140.0*	144.0*	4.0

Note: Δ_{LVDT} = Displacement measured by LVDT, Δ_{DIC} = Displacement measured by DIC, E_{abs}. = Absolute error.

Table 6b
Plasticity parameters of concrete.

Parameter	Value
Dilation angle (ψ)	40
Eccentricity (ε)	0.1
Equibiaxial Compressive yield stress/ Uniaxial compressive yield stress (f_{bo}/f_{co})	1.16
Viscosity Parameter (μ)	0.0005
Constant (K)	0.667

help of strain contours utilizing DIC analysis. The strain contours of all the specimens are presented in **Appendix-1**. Strain contours of HCS tested at a/d ratio of 3.5, 7 and 10 are shown in Fig. 27, Fig. 28 **and** Fig. 29**,** respectively. The strain distribution was determined to investigate the contribution of fibres to crack resistance. The steel rebar yielded before reaching the peak load in the specimens tested at a/d ratios 7 and 10. Hence the key points examined in those specimens are cracking load, load at yielding point, peak load, and load at measured maximum deflection. The specimens tested at an a/d ratio of 3.5, nevertheless failed in shear. In those cases, the rebar did not yield. As a result, loads of 40 kN, 80 kN, 100 kN, and 120 kN are chosen as important values for comparing the strain profiles. A minor crack is observed in strain contours at the cracking load. The number of cracks increased as the load increased. The strain contours in control specimens and fibre-reinforced specimens looked similar. The horizontal strain increased with an increase in load in all specimens. Due to strain localization, the crack initiation occurred at the bottom of the tension zone and progressed towards the top of the compressive force of HCS specimens. In HCS, the jump in strain contours suggests the existence of a crack in that region. The strain contours of control specimens could not be represented at higher loads in the HCS specimens tested at a/d ratio three because the specimens failed at a relatively lower load than fibre-reinforced HCS specimens.

4.5.2. Load vs crack width

The relation between load and crack width is depicted in Fig. 14 as determined by DIC analysis using the process adopted by Lakavath et al. [48]. For each HCS specimen, the crack width is measured at the level of reinforcement. The crack width at the first cracking load for all the specimens is negligible. However, the crack width starts to increase with the increase in load. The crack width of fibre reinforced specimens at a particular load level is lesser than control specimens. For all a/d ratios, the crack width of PO06-HCS is the smallest, followed by PO04-HCS, PO00-HCS, and NCA-HCS for a specific load. However, none of the hollowcore slabs cracked under service loads. The service load calculations for all the HCS are given in Appendix 2.

5. Numerical validation

A valid geometrical and material model which can replicate the experimental response is essential for performing a comprehensive parametric study. A numerical study was carried out by a nonlinear finite element software called ABAQUS and is corroborated by the experimental results. Thus, the model validated can be used to perform parametric studies in future. In the current investigation, the concrete damage plasticity (CDP) model was employed to characterise the nonlinear material behaviour of concrete. The CDP model proposed by Lubliner et al. [50] and elaborated by Lee and Fenves [51] was implemented for the analysis. The two fundamental failure modes that control the CDP model are tensile cracking and compressive crushing. C3D8R, an eight-node solid element, was used to model concrete. Steel rebar was modelled using a truss element (T3D2). Materials properties were assigned to model parts, resulting in a single body. Section steel bars were regarded as a uniaxial material in the element. The mechanical properties of steel rebar include density, elastic modulus, Poisson's ratio and yield strength of 78,000 kg/m^3, 20000 MPa, 0.3 and 550 MPa, respectively. The cracking behaviour of rebars and concrete was considered independently. Convergence issues were avoided using explicit model analysis. Since the concrete's stress–strain properties are separated into elastic and plastic components, the overall strain of concrete is defined by adding the elastic and plastic strains. The plasticity and damage response of concrete are demonstrated through a nonlinear response to a stress–strain curve.

The plasticity parameters assumed for the CDP model such as dilation angle (ψ), eccentricity (ε), the ratio of biaxial yield stress to uniaxial yield stress ($\frac{f_{bo}}{f_{co}}$), viscosity parameter (μ) and the coefficient to obtain the shape of the deviatory cross-section (K) were taken based on ABAQUS user manual [52] and previous literature [53 54] and are presented in Table 6a and 6b. Compressive stress–strain curves (Fig. 15**.**) discussed in the authors' previous research [8], and tensile stress–strain curves (Fig. 16**.**) presented in the authors' previous paper [11] were used in the

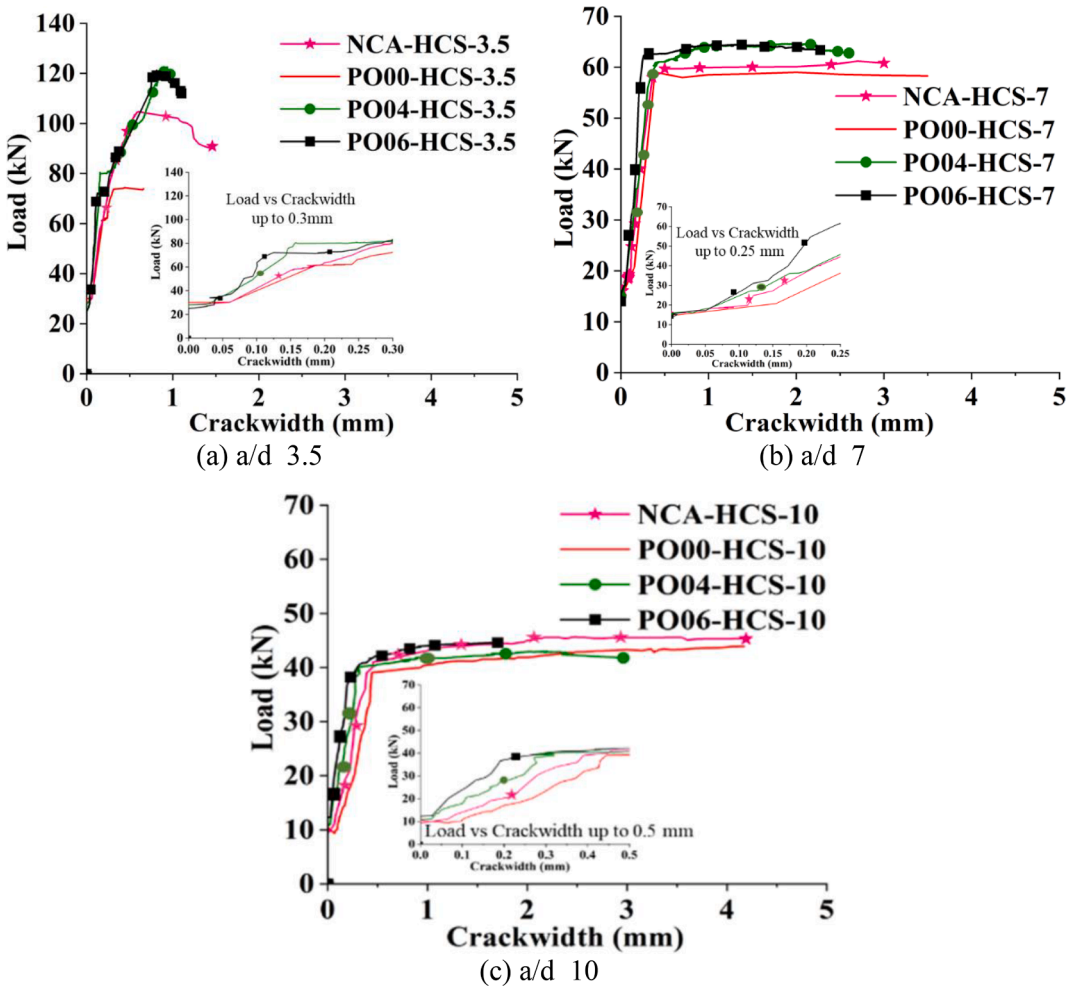

Fig. 14. Load vs Crack width.

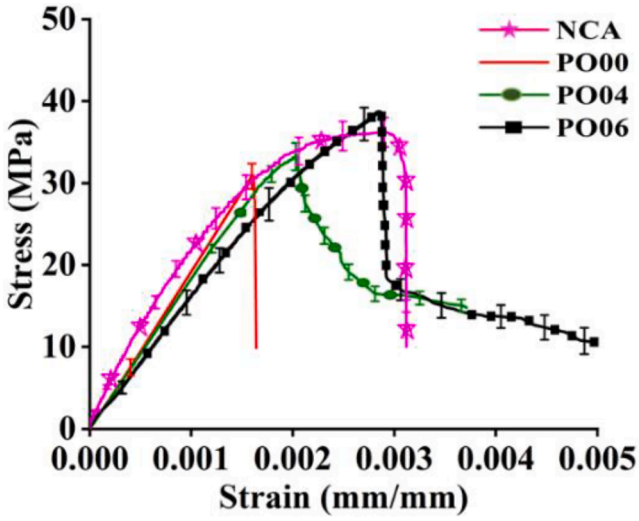

Fig. 15. Stress–strain curve for compression.

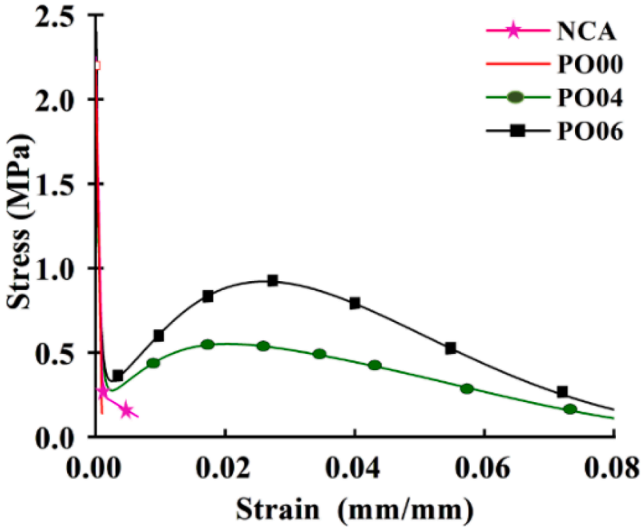

Fig. 16. Stress–strain curve for tension.

analysis. The tensile stress–strain curve for FR-SLWAC with the varying dosage of synthetic fibres was predicted using the stress-crack width model and inverse analysis. The stress-crack width model is established using the load-CMOD (Crack mouth opening displacement) curve obtained from the fracture test. More details regarding the stress-crack width analysis and prediction of the tensile constitutive relationship can be found in the companion paper of the author [11]. The stress–-strain behaviour of Fe550 rebar is depicted in Fig. 17.

Finite element models were created for all HCS specimens and analysed at a/d ratios of 3.5, 7, and 10. Meshing is a crucial stage in

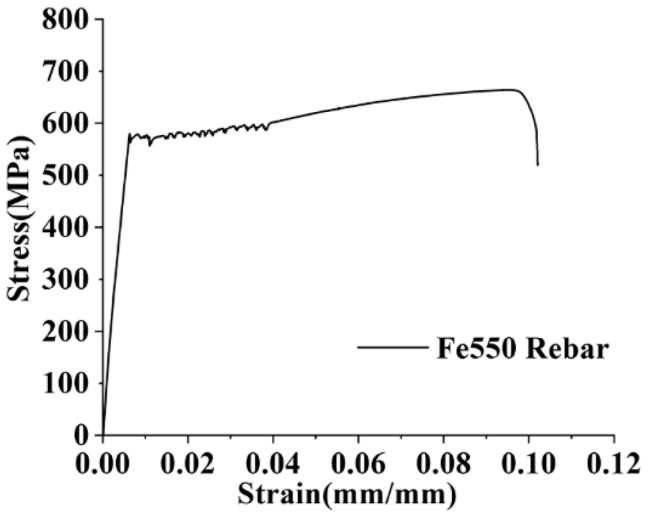

Fig. 17. Stress–strain curve for Fe550 rebar.

numerical modelling since the accuracy of predictions can only be improved by selecting an appropriate mesh type. For the investigation, an optimum mesh size of 30 mm was chosen after performing a mesh convergence study. The mesh of FE analysis is represented in Fig. 18. The boundary conditions of the FEMs were carefully matched to the experimental test conditions. Nodes at the top surface were displaced downward at a distance from support nodes (according to different a/d ratios). Similar to a displacement-controlled load application in the experiment, the entire line of nodes was deflected downward till the slab failed. The maximum deflection applied to each HCS specimen in the FE model was the same as the maximum measured deflection from the test results.

5.1. Comparison of Load-Deflection behaviour

To validate the correctness of the FE model, the predictions were compared to the experimental findings of the HCS tested at different a/d ratios. The load–deflection behaviour of the HCS specimens obtained from the experiment and FE model is depicted in Fig. 19. The proposed model closely approximates the load–deflection behaviour obtained from the test results. The variation in peak load between the experimental and finite element analysis load–deflection curves is around 10 %. For most specimens, the FE results are slightly overestimating the cracking load. However, the overall behaviour is captured with reasonable accuracy. Additionally, to understand the validity of the developed model, the moment–curvature response of experimental and FE analysis was also compared in Fig. 20**.** It is observed that the curves are in good agreement with each other. Only the result for PO04-HCS is shown to maintain the brevity of the paper.

5.2. Comparison of failure modes

The developed FE models effectively captured failure mechanisms. The final failure modes of developed FE models are compared with experimental failure modes shown in Fig. 21. Shear cracks were seen in the specimen tested with an a/d ratio of 3.5, and the main cracks formed at the shear span. Specimens examined with a/d ratio 7 showed both flexure and shear cracks. Flexural cracks, however, were seen in the specimen tested at an a/d ratio of 10. The main cracks were formed at a constant moment zone of the slab. Thus, finite element models accurately predicted the crack patterns and failure phenomenon. The number of cracks in the FE analysis will also differ from the number of cracks in the experiments. The numerical models in the FE package do not directly show physical cracking, but the maximum plastic tensile strain can be used to refer to the potential cracking pattern [55].

5.3. Summary of experimental and FE results

Table 7 compares the important parameters from FE analysis with test results. The cracking load, peak load, and energy absorption capacity are critical metrics for comparing experimental and FE observations. The cracking load difference between NCA-HCS-3.5 and PO00-HCS-3.5 is 5 %. However, there is a 25 % margin in the case of PO04-HCS-3.5 and PO06-HCS-3.5. Peak load varies by around 10 % in specimens tested at an a/d ratio of 3.5. Except for PO00-HCS-7 and PO04-HCS-7, the cracking load of specimens examined at the a/d ratio is relatively same. Despite this, the difference in peak load and energy absorption capacity of specimens evaluated at a/d ratios is less than 10 %. Except for NCA-HCS-10, the specimens examined at a/d ratio 10

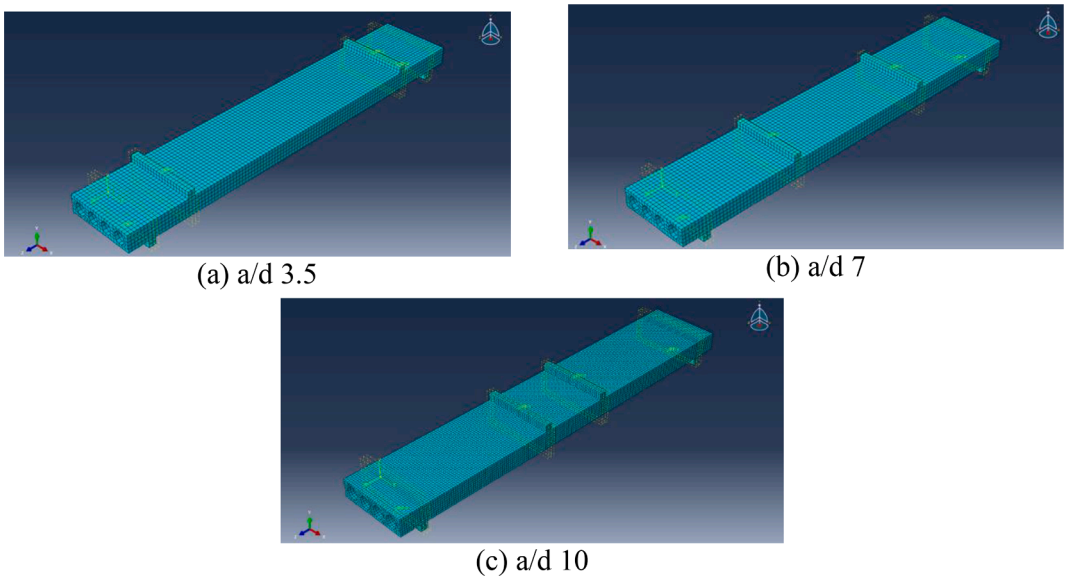

Fig. 18. Mesh for finite element analysis.

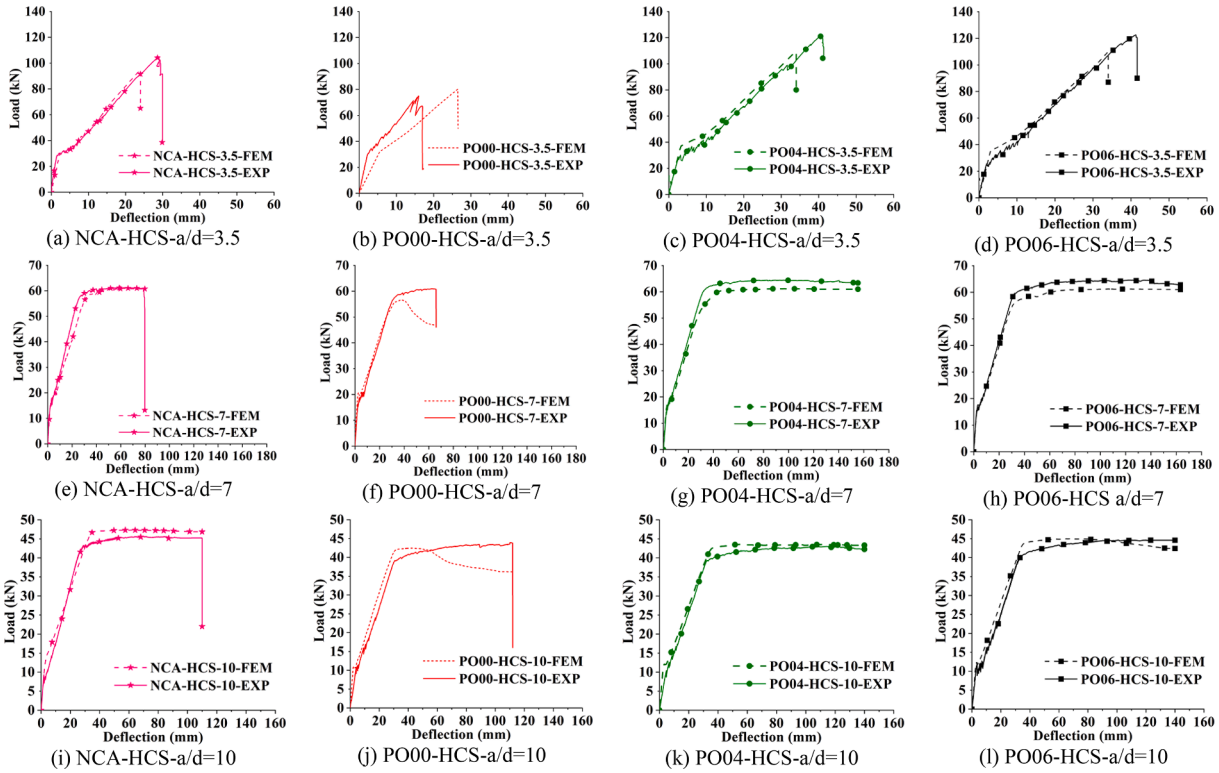

Fig. 19. Comparison of load–deflection behaviour (Experimental vs FEM).

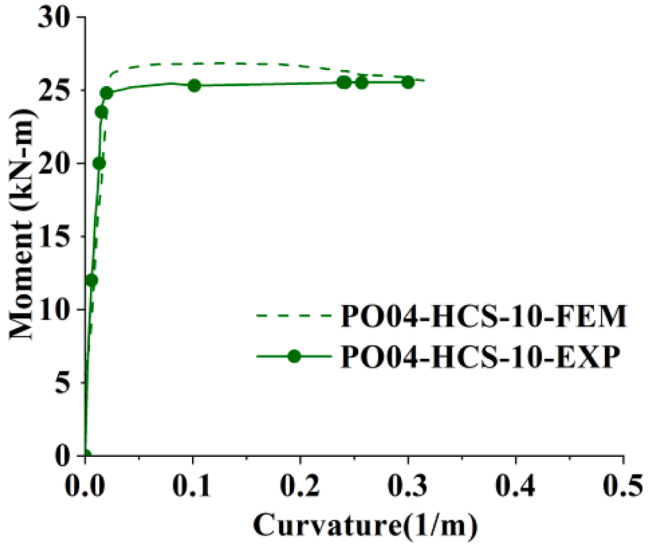

Fig 20. Moment vs Curvature comparison between experimental and FE results.

provide the best prediction in cracking load, peak load, and energy absorption capacity, with differences within 5 %.

5.4. Parametric studies

The parametric studies taken into account are the effects of changing the reinforcement, the slab's depth, and the a/d ratio. However, the parametric study results of only PO04-HCS have been included to maintain brevity. To study the impact of a change in the tensile reinforcement ratio, reinforcement bars with diameters of 8 mm, 10 mm, and 12 mm corresponding to reinforcement ratios of 0.45 %, 0.7 %, and 1 % are taken into consideration. The a/d ratios of 2, 3.5, 5, 7, 8.5, and 10 are considered to study the impact of different a/d ratios on the load–deflection behaviour of HCS. Additionally, the failure modes at the a/d ratios previously mentioned are also evaluated.

The effect of change in reinforcement ratio on load–deflection behaviour of HCS is illustrated in Fig. 22. This study took into account steel rebar with a 10 mm diameter. When the rebar diameter was increased to 12 mm in the a/d ratio 3.5 (Fig. 22 **(a)**), the cracking and peak loads increased by 7 % and 5 %, respectively. When the rebar diameter was decreased to 8 mm, the cracking and peak loads both decreased by 8 % and 14 %, respectively. Additionally, it was found that as rebar diameter increased, the deflection at failure load decreased. Similarly, at a/d ratio 7 (Fig. 22 **(b)**), the cracking load and peak load increased by 35 % and 40 %, respectively, when 12 mm diameter rebar was used compared to 10 mm diameter rebar. The cracking load and peak load decreased by 8 % and 50 %, respectively in 8 mm dia bar when compared to specimen with 10 mm diameter rebar. Similar to this, at an a/d ratio of 10 (Fig. 22 **(c)**), the cracking load and peak load of 12 mm diameter rebar increased by 8 % and 38 %, respectively, in comparison to a 10 mm diameter bar. The cracking and peak loads decreased by 9 % and 45 %, respectively in speicmens with 8 mm diameter bar as compared to the ones 10 mm diameter bar.

The impact of change in depth on the load–deflection behaviour of HCS is depicted in Fig. 23. This study took into account the depth of HCS as 150 mm. When the slab's depth was increased to 175 mm and 200 mm at an a/d ratio of 3.5 (Fig. 23 **(a)**), the cracking load was found to have increased by 50 % and 100 %, respectively, and the peak load was found to have increased by 27 % and 63 %, respectively when compared with 150 mm depth HCS. Similarly, at a/d ratio of 7 (Fig. 23 **(b)**), the cracking load increased by 40 % and 100 % for 175 mm depth and 200 mm depth, respectively. However, the peak load increased by 27 % and 54 %, respectively when compared to HCS with 150 mm depth. Similar to this, at an a/d ratio of 10 (Fig. 23 **(c)**), the cracking load increased by

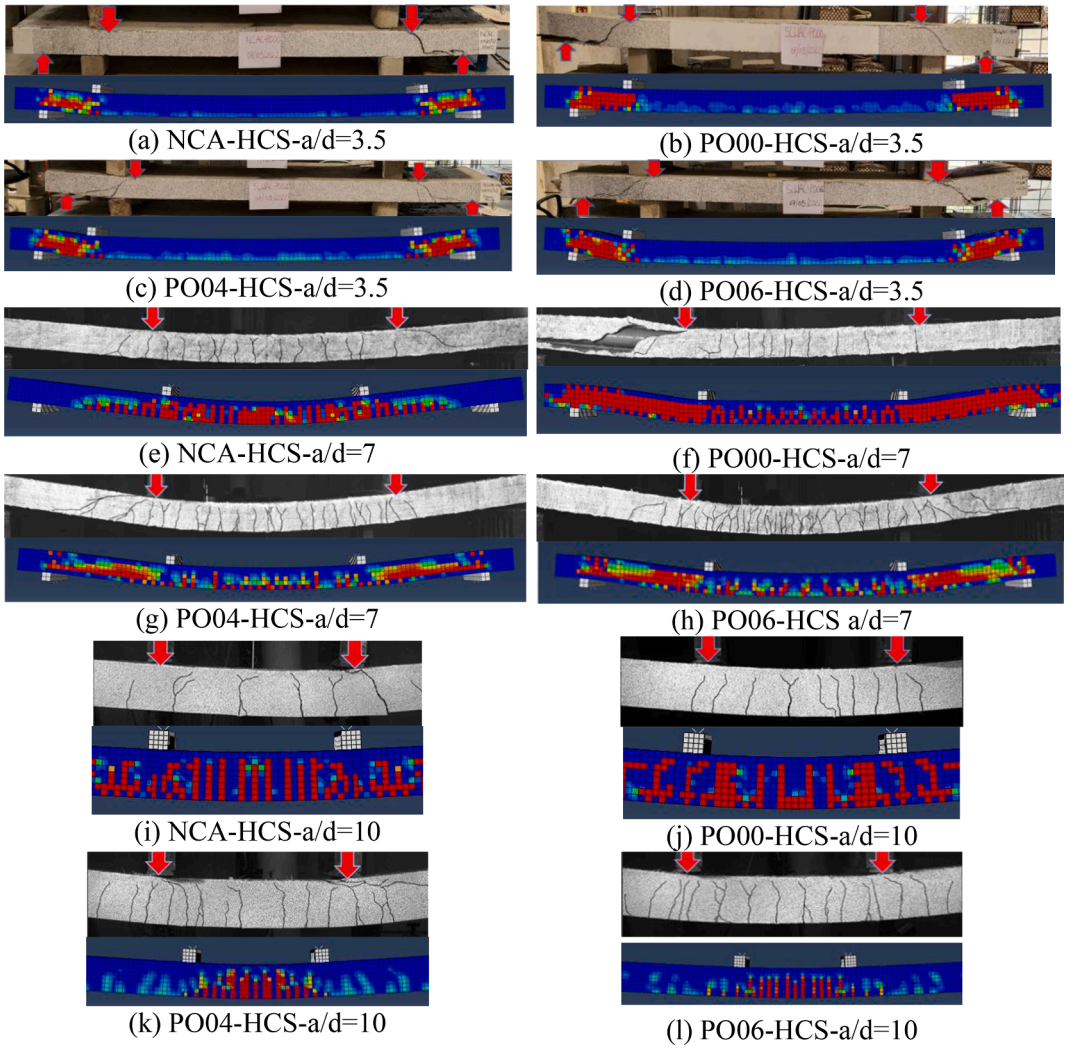

Fig. 21. Comparison of failure modes (Experimental vs FEM).

Table 7
Summary of experimental and FEM results.

Specimen ID	CL_{EXP}(kN)	CL_{FEM}(kN)	PL_{EXP}(kN)	PL_{FEM}(kN)	SE_{EXP}(Joule)	SE_{FEM}(Joule)	$\frac{CL_{EXP}}{CL_{FEM}}$	$\frac{PL_{EXP}}{PL_{FEM}}$	$\frac{EA_{EXP}}{EA_{FEM}}$
NCA-HCS-3.5	28.4	30.4	102.5	95.0	1880.2	1324.8	0.93	1.07	1.41
PO00-HCS-3.5	30.7	32.0	75.0	80.0	816.5	1250.4	0.96	0.94	0.65
PO04-HCS-3.5	28.5	37.2	121.4	110.0	2871.0	2209.8	0.77	1.10	1.30
PO06-HCS-3.5	25.6	35.2	122.6	110.0	2977.0	2200.3	0.73	1.12	1.35
NCA-HCS-7	15.5	16.0	61.2	61.0	4130.2	3983.4	0.97	1.01	1.03
PO00-HCS-7	16.4	20.4	60.9	56.6	3148.0	2864.8	0.80	1.07	1.10
PO04-HCS-7	14.4	17.0	64.4	61.1	8019.0	7598.0	0.85	1.05	1.05
PO06-HCS-7	15.6	15.5	65.1	61.2	7978.0	7585.0	1.01	1.06	1.05
NCA-HCS-10	9.3	13.5	45.6	47.3	4535.2	4357.3	0.69	0.96	1.04
PO00-HCS-10	10.7	10.9	43.9	42.4	4105.0	3938.8	0.98	1.03	1.04
PO04-HCS-10	10.4	11.7	43.0	43.5	5233.0	5418.5	0.88	0.99	0.96
PO06-HCS-10	12.2	12.1	44.6	44.9	5404.0	5515.0	1.01	0.99	0.98

Note: CL_{EXP} = Experimental cracking load, CL_{FEM} = Predicted cracking load using FEM,PL_{EXP} = Experimental peak load, PL_{EXP} = Predicted peak load using FEM, EA_{EXP} = experimental energy absorption capacity, EA_{FEM} = Energy absorption capacity using FEM.

42 % and 96 % for 175 mm depth and 200 mm depth, respectively. However, the peak load was increased by 27 % and 50 % respectively as compared to the 150 mm depth of HCS.

To investigate the effect of change in a/d ratio on the load–deflection behavior of PO04-HCS, a total of six a/d ratios such as 2, 3.5, 5, 7, 8.5 and 10 are considered. The cracking and peak loads increased when the a/d ratios increased. PO04-HCS had a 12 kN cracking load at an a/d ratio of 2. The cracking load increased by 13 %, 40 %, 100 %, 230 %, and 430 %, respectively, at a/d ratios of 3.5, 5, 7, 8.5, and 10 in comparison to a/d ratio 2. The peak load of PO04-HCS at an a/d ratio of 2

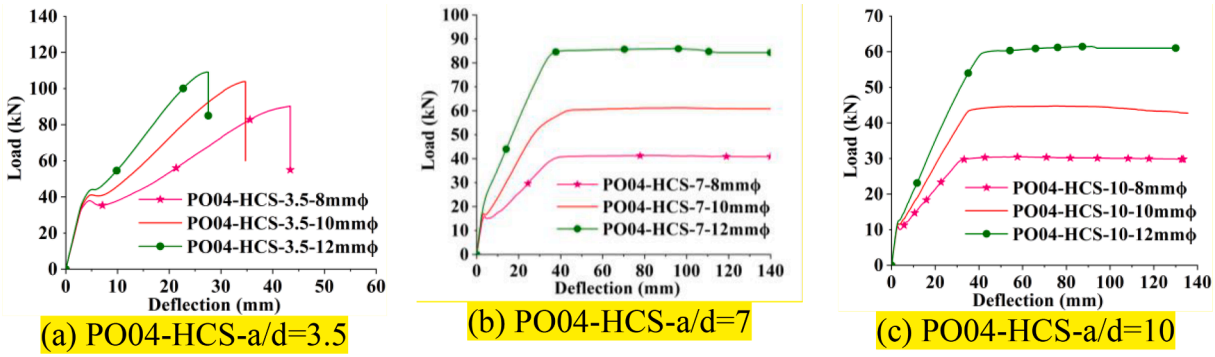

Fig. 22. Effect of change in tensile reinforcement ratio on load–deflection behaviour.

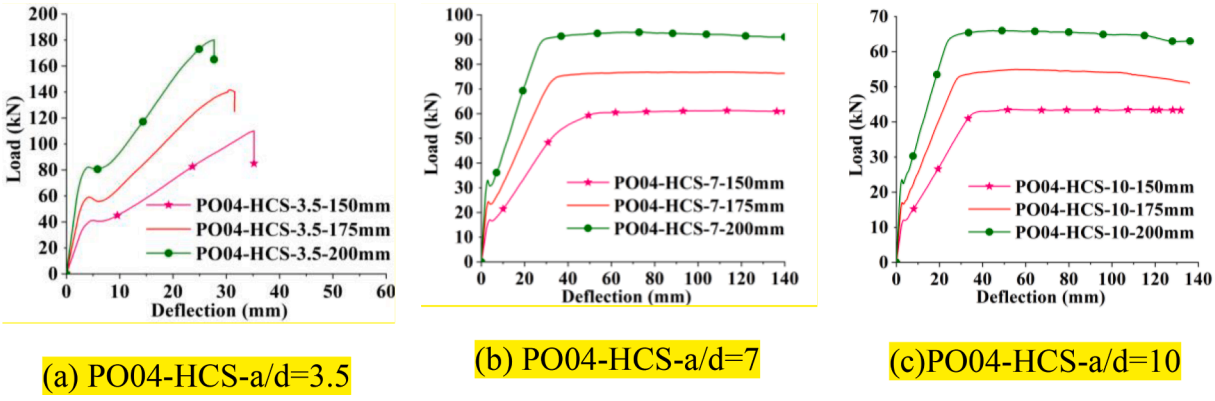

Fig. 23. Effect of change in depth of slab on load–deflection behaviour.

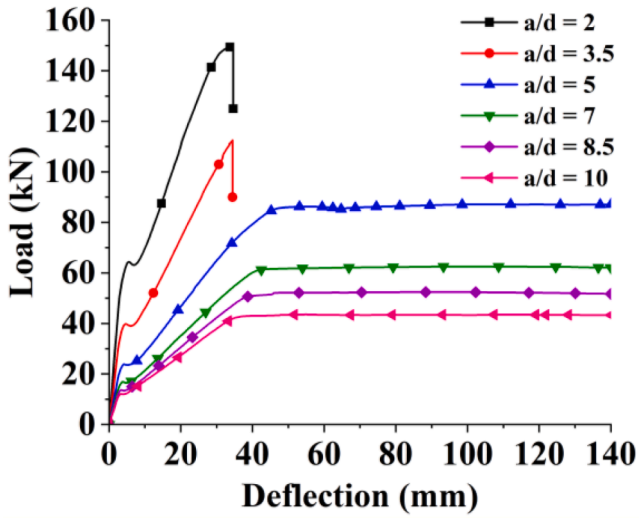

Fig. 24. Effect of change in a/d ratio on load–deflection behaviour.

was 43.4 kN. The cracking load increased by 24 %, 44 %, 100 %, 160 % and 250 %, respectively at a/d ratios of 3.5, 5, 7, 8.5 and 10 when compared with an a/d ratio of 2. Fig. 24 shows the effect of change in the a/d ratio on load–deflection behavior.

The failure modes of PO04-HCS are shown in Fig. 25 at various a/d ratios. The specimen failed in shear at a/d ratios of 2 and 3.5. At a/d ratios of 5 and 7, the specimen failed in the flexural shear mode. However, at a/d ratios of 8.5 and 10, the specimens failed in the flexure mode.

Fig. 26 shows the effect of a/d ratio on the behavior of PO04-HCS. The ratio of ultimate moment at failure and pure flexural capacity (M_u/M_{fl}) is plotted against a/d ratio. For the specimens tested in the study, the ratio of M_u/M_{fl} increased with the increase in a/d ratio unlike what was observed by Kani [33]. The specimens tested in the study failed in shear mode at a/d ratio of less than 3.5. However, it failed in flexural mode at a/d ratio higher than 7. Furthermore, the specimens failed in flexural shear mode at a/d ratio between 3.5 and 7. However, it does not follow the trend observed by Kani. It is worth mentioning that Kani tested rectangular beams with different sectional parameters than the ones reported in the study. HCS specimens tested in the study can become deficient in shear under low a/d ratios, because of the lesser concrete area in the web region. As a result, before reaching the flexural capacity, the specimen tested at an a/d ratio of less than 3.5 failed in shear. So, for a constant depth, M_u/M_{fl} for HCS specimens which failed in shear are lesser than that of specimens that failed in flexural-shear. This signifies Kani's failure criteria are strictly not valid for light-weight hollow core slabs.

6. Summary and conclusions

The behaviour of fibre reinforced lightweight hollow core slabs at varying a/d ratios such as 3.5, 7 and 10 were studied. The behaviour of

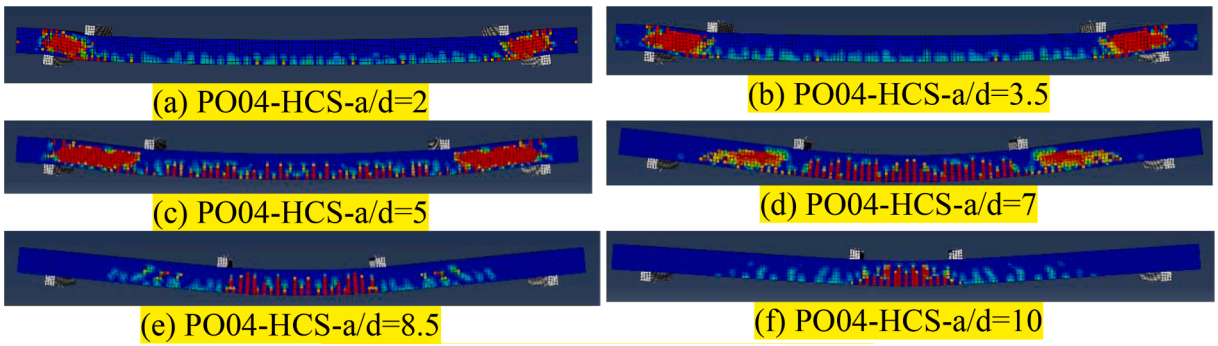

Fig.25. Failure modes at different a/d ratio.

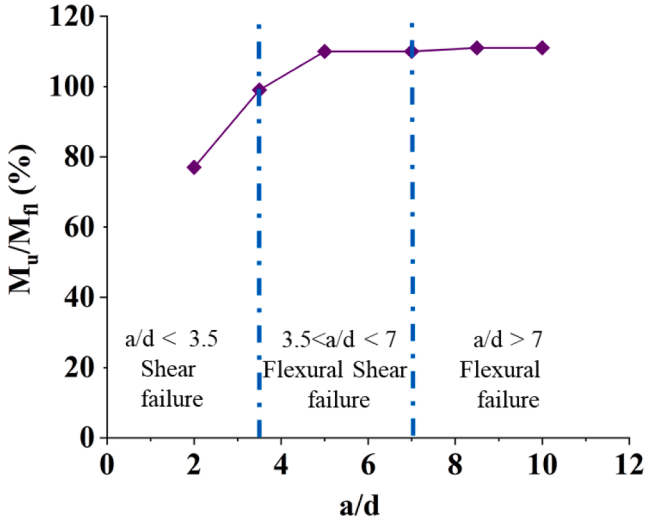

Fig. 26. Effect of a/d ratio on the behaviour of PO04-HCS.

fibre reinforced, and control specimens were compared. The crack patterns and failure modes were examined at different a/d ratios. The limited findings presented in this study can lead to the following conclusions.

I. Fibres inhibited crack development and propagation and improved energy absorption of fibre-reinforced lightweight HCS at all a/d ratios.
II. Adding 0.6 % fibre dosage to control HCS specimens enhanced peak load by 60 % at an a/d ratio of 3.5. However, the fibre contribution to shear resistance is marginal. The failure was brittle and abrupt.
III. The load–deflection curves of HCS specimens evaluated at a/d ratios 7 and 10 showed a similar pattern. However, the addition of fibres did not significantly enhance peak load at these a/d ratios but significantly boosted energy absorption capacity. The failure in a/d ratios 7 and 10 was more ductile than in specimens tested at an a/d ratio of 3.5.
IV. The load–strain curve demonstrates that the strain at a given load for FR-LWHCS is smaller than that of LWHCS, indicating active fibre engagement.
V. The DIC results showed that fibre-reinforced HCS specimens had less crack width than the HCS specimens without fibres at a given load demonstrating the efficacy of fibres in inhibiting crack development.
VI. All the HCS remain uncracked at design service loads indicating the superior serviceability performance of the HCS.
VII. The load–deflection behaviour and failure modes obtained using ABAQUS finite element model were validated against

Appendix-1

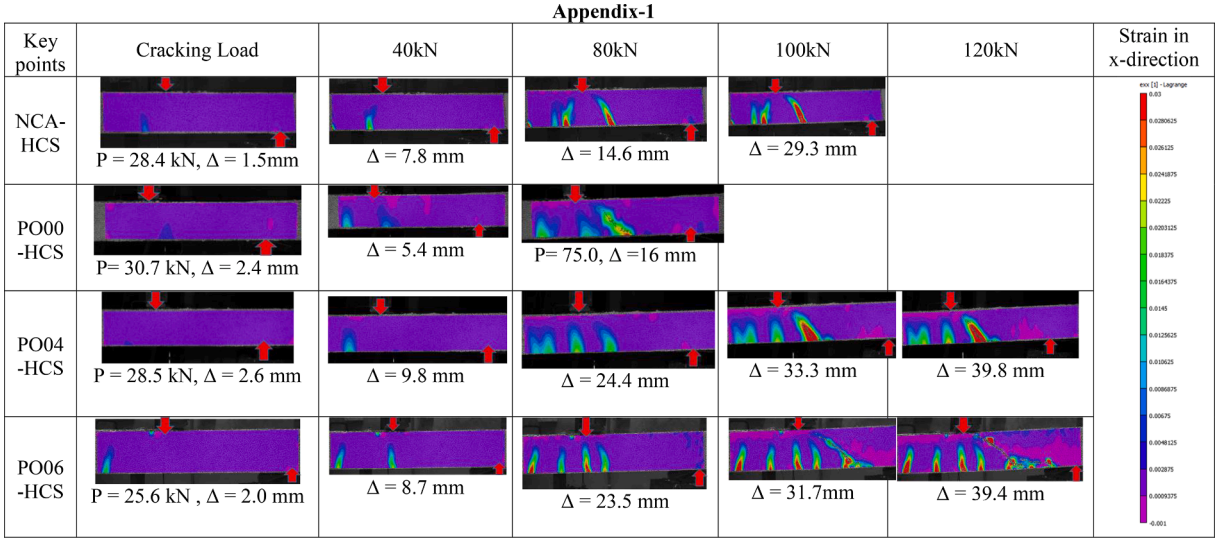

Fig. 27. Strain contours of HCS tested at a/d ratio 3.5.

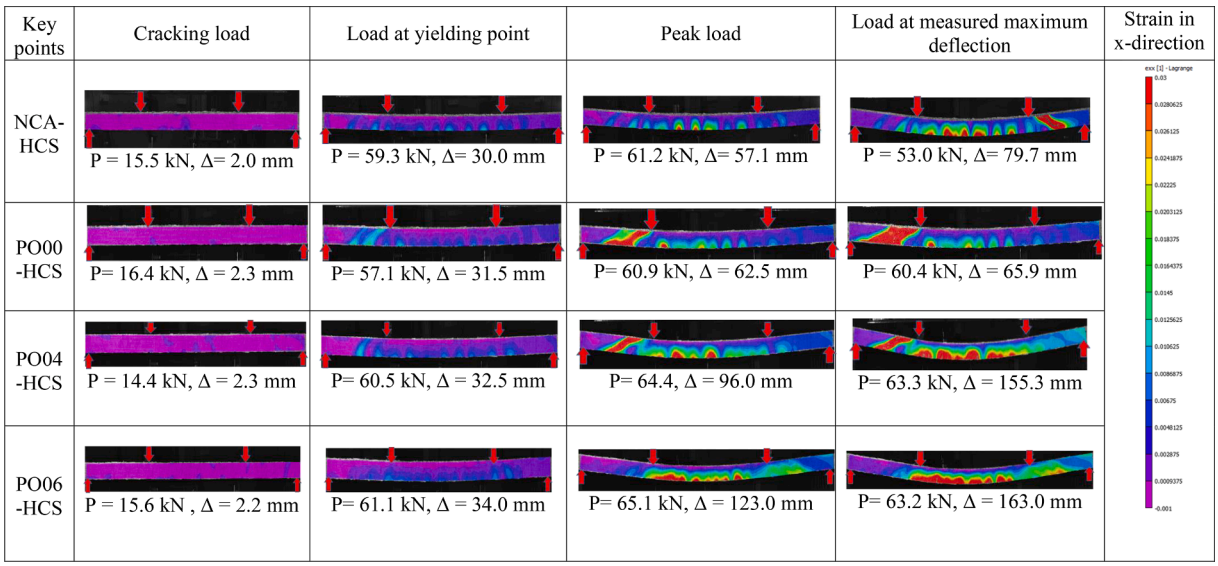

Fig. 28. Strain contours of HCS tested at a/d ratio 7.

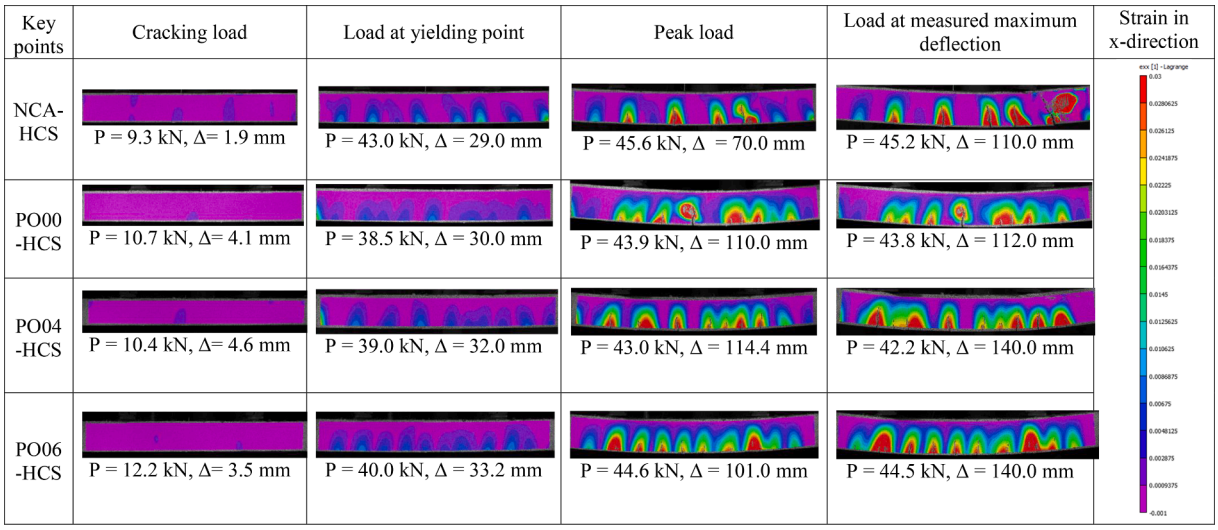

Fig. 29. Strain contours of HCS tested at a/d ratio 10.

experimental observations. The finite element findings were in good agreement with the experimental test results.

VIII. The results of the parametric analysis show that hollow core slabs failed in shear at a/d ratios between 2 and 3.5, in flexural shear at a/d ratios between 3.5 and 7, and in flexure at a/d ratios greater than 7. However, they do not follow the trend observed in the classical work of Kani.

CRediT authorship contribution statement

Sumit Sahoo: Conceptualization, Methodology, Investigation, Validation, Writing – original draft. **Chetharajupalli Veerendar:** Methodology, Investigation, Software, Validation, Formal analysis. **Nikesh Thammishetti:** Formal analysis, Writing – review & editing. **S Suriya Prakash:** Data curation, Supervision, Writing – review & editing.

Declaration of Competing Interest

The authors declare that they have no known competing financial interests or personal relationships that could have appeared to influence the work reported in this paper.

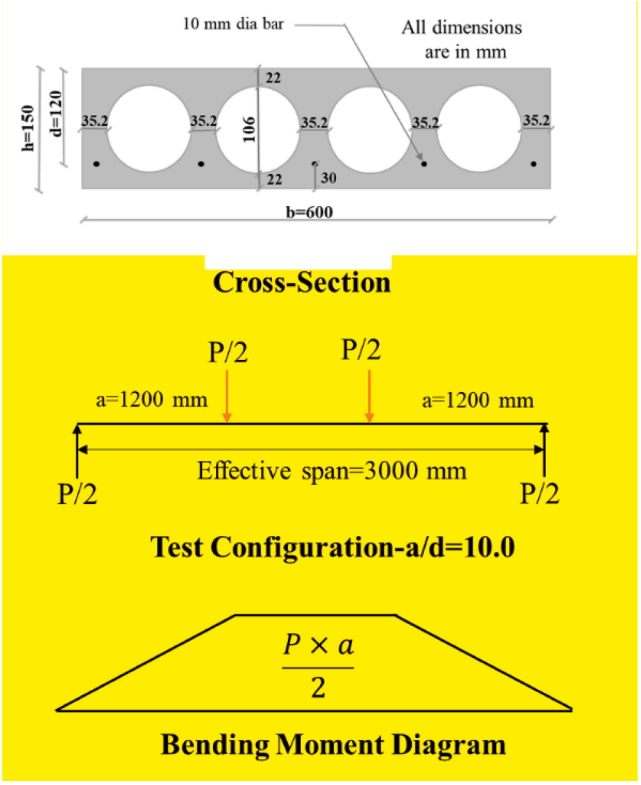

Fig. 30. Cross-section detail, Loading configuration and Bending moment diagram of HCS.

Acknowledgements

This research work was sponsored by "IMPRINT Scheme- Order # IMP/2018/000846" funded by Ministry of Human Resource Development and Department of Science and Technology, India. The authors would like to thank the funding agency for their generous support.

Appendix 1

Appendix 2

Calculation of design service load:

Cross-sectional area of HCS $=.(0.6m \times 0.15m) - \left(4 \times \frac{\pi}{4} \times 0.106^2 m^2\right) = 0.055m^2$

For PO00-HCS, PO04-HCS and PO06-HCS the density of concrete is taken as $1800Kg/m^3$.

Self-weight of the HCS $=.\left(0.055m^2 \times 1800Kg/m^3 \times 9.81m/s^2\right) = 0.97kN/m$

Typical super-imposed loads in residential applications$=.\left(1.5kN/m^2 \times 0.6m\right) = 0.9kN/m$

Weight of screed flooring $=.\left(0.075m/m \times 25kN/m^2 \times 0.6m\right) = 1.125kN/m$

Typical live loads in residential applications $= \left(3kN/m^2 \times 0.6m\right) = 1.80kN/m$ [56].

Total service load (w) $=.(0.97+0.9+1.125+1.8)kN/m = 4.8kN/m$

Bending moment (demand) in service $= \frac{wl^2}{8} = \frac{4.8\frac{kN}{m} \times (3.0m)^2}{8} = .5.4kNm$

Design service load from four-point bending test configuration (P):

$$\frac{P}{2} \times 1.2 = 5.4kNm; P = 9kN$$

It is calculated that PO00-HCS, PO04-HCS, and PO06-HCS have a service load of 9 kN each.

For NCA-HCS, the density of concrete $2400Kg/m^3$ is used in the calculation keeping all other parameters the same and the design service load (P) is estimated to be 9.6 kN.

The cross-section, test configuration and bending moment diagram of HCS is shown in Fig. 30. An a/d ratio of 10 is used in the calculation to conservatively estimate the service loads.

References

[1] Nassif Sabr Y, Khalaf Jarallah H, Issa AbdulKareem H. Improving Shear Strength of Thick Hollow Core Slabs By Using Lightweight High Strength Concrete Produced From Recycled Crushed Clay Brick and Iron Powder Waste. J Eng Sustain Dev 2019;23:128–46. https://doi.org/10.31272/jeasd.23.6.10.

[2] Al-Shaarbaf IA, Al-Azzawi AA, Abdulsattar R. A state of the art review on hollow core slabs. ARPN J Eng Appl Sci 2018;13:3240–5.

[3] Al-Azzawi AA, Abdul Al-Aziz BM. Numerical analysis of reinforced lightweight aggregate concrete hollow core slabs, ARPN. J Eng Appl Sci 2017;12:1743–57.

[4] Rossignolo JA, Agnesini MVC, Morais JA. Properties of high-performance LWAC for precast structures with Brazilian lightweight aggregates. Cem Concr Compos 2003;25:77–82. https://doi.org/10.1016/S0958-9465(01)00046-4.

[5] Agrawal Y, Gupta T, Sharma R, Panwar NL, Siddique S. A Comprehensive Review on the Performance of Structural Lightweight Aggregate Concrete for Sustainable Construction. Constr Mater 2021;1:39–62. https://doi.org/10.3390/constrmater1010003.

[6] Gomathi P, Sivakumar A. Accelerated curing effects on the mechanical performance of cold bonded and sintered fly ash aggregate concrete. Constr Build Mater 2015;77:276–87. https://doi.org/10.1016/j.conbuildmat.2014.12.108.

[7] Satpathy HP, Patel SK, Nayak AN. Development of sustainable lightweight concrete using fly ash cenosphere and sintered fly ash aggregate. Constr Build Mater 2019;202:636–55. https://doi.org/10.1016/j.conbuildmat.2019.01.034.

[8] Sahoo S, Selvaraju AK, Suriya Prakash S. Mechanical characterization of structural lightweight aggregate concrete made with sintered fly ash aggregates and synthetic fibres. Cem Concr Compos 2020;113:103712.

[9] Nadesan MS, Dinakar P. Mix design and properties of fly ash waste lightweight aggregates in structural lightweight concrete, Case Stud. Constr Mater 2017;7:336–47. https://doi.org/10.1016/j.cscm.2017.09.005.

[10] Hassanpour M, Shafigh P, Bin Mahmud H. Lightweight aggregate concrete fiber reinforcement - A review. Constr Build Mater 2012;37:452–61. https://doi.org/10.1016/j.conbuildmat.2012.07.071.

[11] Sahoo S, Lakavath C, Prakash SS. Experimental and Analytical Studies on Fracture Behavior of Fiber-Reinforced Structural Lightweight Aggregate Concrete. J Mater Civ Eng 2021;33:04021074. https://doi.org/10.1061/(asce)mt.1943-5533.0003680.

[12] Rasheed MA, Prakash SS. Behavior of hybrid-synthetic fiber reinforced cellular lightweight concrete under uniaxial tension – Experimental and analytical studies. Constr Build Mater 2018;162:857–70. https://doi.org/10.1016/j.conbuildmat.2017.12.095.

[13] Enfedaque A, Alberti M, Gálvez J. Influence of fiber distribution and orientation in the fracture behavior of polyolefin fiber-reinforced concrete. Materials (Basel) 2019;12(2):220.

[14] Natalli JF, Andrade HD, Carvalho JMF, Defáveri K, Castro Mendes J, Sarmanho AMC, et al. Performance of Lightweight Concrete with Expansive and Air-Entraining Admixtures in CFST Columns. J Mater Civ Eng 2020;32. https://doi.org/10.1061/(ASCE)MT.1943-5533.0003143.

[15] Kankeri P, Pachalla SKS, Thammishetti N, Prakash SS. Behavior Of Structural Macrosynthetic Fiber-Reinforced Precast, Prestressed Hollow-Core Slabs at Different Flexure-to-Shear Ratios. PCI J 2019;64:76–91. https://doi.org/10.15554/pcij64.3-01.

[16] Lee C-H, Mansouri I, Kim E, Hwang K-S, Woo W-T. Flexural Strength of One-Way Composite Steel Deck Slabs Voided by Circular Paper Tubes. J Struct Eng 2019;145:04018246. https://doi.org/10.1061/(asce)st.1943-541x.0002259.

[17] Wariyatno NG, Haryanto Y, Sudibyo GH. Flexural Behavior of Precast Hollow Core Slab Using PVC Pipe and Styrofoam with different Reinforcement. Procedia Eng 2017;171:909–16. https://doi.org/10.1016/j.proeng.2017.01.388.

[18] Azad AK, Hakeem IY. Flexural behavior of hybrid hollow-core slab built with ultra high performance concrete faces. Mater Struct Constr 2016;49:3801–13. https://doi.org/10.1617/s11527-015-0755-7.

[19] Jiang Q, Wang H, Feng Y, Chong X, Huang J, Zhang K, et al. Out-of-plane flexural performance of concrete composite wide flat beam with hollow-core slabs. Structures 2022;41:629–42. https://doi.org/10.1016/j.istruc.2022.05.054.

[20] Naser FH, Al Mamoori AHN, Dhahir MK. Effect of using different types of reinforcement on the flexural behavior of ferrocement hollow core slabs embedding PVC pipes, Ain Shams Eng. J 2021;12(1):303–15.

[21] Brunesi E, Bolognini D, Nascimbene R. Evaluation of the shear capacity of precast-prestressed hollow core slabs: numerical and experimental comparisons. Mater Struct 2015;48:1503–21. https://doi.org/10.1617/s11527-014-0250-6.

[22] Rahman MK, Baluch MH, Said MK, Shazali MA. Flexural and Shear Strength of Prestressed Precast Hollow-Core Slabs. Arab J Sci Eng 2012;37:443–55. https://doi.org/10.1007/s13369-012-0175-8.

[23] Conforti A, Ortiz-Navas F, Piemonti A, Plizzari GA. Enhancing the shear strength of hollow-core slabs by using polypropylene fibres. Eng Struct 2020;207:110172. https://doi.org/10.1016/j.engstruct.2020.110172.

[24] Sales MWR, Ferreira MdA, Araújo DdL. Evaluation of shear strength of pre-stressed hollow core slab. Structures 2022;38:1465–82.

[25] Simasathien S, Chao SH. Shear strength of steel-fiber-reinforced deep hollow-core slabs. PCI J 2015;60:85–101. https://doi.org/10.15554/pcij.07012015.85.101.

[26] Cuenca E, Serna P. Failure modes and shear design of prestressed hollow core slabs made of fiber-reinforced concrete. Compos Part B Eng 2013;45:952–64. https://doi.org/10.1016/j.compositesb.2012.06.005.

[27] Pajari M. Resistance of prestressed hollow core slabs against web shear failure, VTT Tied. - Valt Tek Tutkimusk 2005:3–47.

[28] Pisanty A. The shear strength of extruded hollow-core slabs. Mater Struct 1992;25:224–30. https://doi.org/10.1007/BF02473067.

[29] Ortiz Navas F, Navarro-Gregori J, Leiva Herdocia G, Serna P, Cuenca E. An experimental study on the shear behaviour of reinforced concrete beams with macro-synthetic fibres. Constr Build Mater 2018;169:888–99. https://doi.org/10.1016/j.conbuildmat.2018.02.023.

[30] Altoubat S, Yazdanbakhsh A, Rieder KA. Shear behavior of macro-synthetic fiber-reinforced concrete beams without stirrups. ACI Mater J 2009;106:381–9. https://doi.org/10.14359/56659.

[31] Dev A, Chellapandian M, Prakash SS. Effect of Macrosynthetic and Hybrid Fibers on Shear Behavior of Concrete Beams Reinforced with GFRP Bars. J Bridg Eng 2020;25:04020031. https://doi.org/10.1061/(asce)be.1943-5592.0001557.

[32] Palmer KD, Schultz AE. Experimental investigation of the web-shear strength of deep hollow-core units. PCI J 2011;56:83–104. https://doi.org/10.15554/pcij.09012011.83.104.

[33] Kani G. How safe are our large concrete beams. Proc: ACI J; 1967.

[34] Pajari M. Web shear failure in prestressed hollow core slabs. J Struct Mech 2009;42:208–17.

[35] Li HT, Deeks AJ, Liu LX, Huang DS, Su XZ. Moment transfer factors for column-supported cast-in-situ hollow core slabs. J Zhejiang Univ Sci A 2012;13:165–73. https://doi.org/10.1631/jzus.A1100170.

[36] Kankeri P, Suriya Prakash S, Pachalla SKS. Experimental and Numerical Studies on Efficiency of Hybrid Overlay and Near Surface Mounted FRP Strengthening of Pre-cracked Hollow Core Slabs. Structures 2018;15:1–12. https://doi.org/10.1016/j.istruc.2018.05.003.

[37] Liu X, Liu Y, Wu T, Wei H. Bond-slip properties between lightweight aggregate concrete and rebar. Constr Build Mater 2020;255:119355. https://doi.org/10.1016/j.conbuildmat.2020.119355.

[38] Jin L, Jiang X-A, Xia H, Chen F, Du X. Size effect in shear failure of lightweight concrete beams wrapped with CFRP without stirrups: Influence of fiber ratio. Compos Part B Eng 2020;199:108257.

[39] Xu L, Li B, Ding X, Chi Y, Li C, Huang B, et al. Experimental Investigation on Damage Behavior of Polypropylene Fiber Reinforced Concrete under Compression. Int J Concr Struct Mater 2018;12. https://doi.org/10.1186/s40069-018-0302-3.

[40] Chi Y, Yu M, Huang L, Xu L. Finite element modeling of steel-polypropylene hybrid fiber reinforced concrete using modified concrete damaged plasticity. Eng Struct 2017;148:23–35. https://doi.org/10.1016/j.engstruct.2017.06.039.

[41] American Society for Testing and Materials. ASTM C33–03: Standard Specification for Concrete Aggregate. ASTM Stand B 2001;04:1–11.

[42] Astm. Standard Specification for Lightweight Aggregates for Structural Concrete. Stand Specif Light Aggregates Struct Concr 2000;04:3–6. https://doi.org/10.1520/C0330.

[43] Rasheed MA, Prakash SS. Mechanical behavior of sustainable hybrid-synthetic fiber reinforced cellular light weight concrete for structural applications of masonry. Constr Build Mater 2015;98:631–40. https://doi.org/10.1016/j.conbuildmat.2015.08.137.

[44] Bhosale AB, Lakavath C, Suriya Prakash S. Multi-linear tensile stress-crack width relationships for hybrid fibre reinforced concrete using inverse analysis and digital image correlation. Eng Struct 2020;225:111275. https://doi.org/10.1016/j.engstruct.2020.111275.

[45] Joshi SS, Thammishetti N, Prakash SS. Efficiency of steel and macro-synthetic structural fibers on the flexure-shear behaviour of prestressed concrete beams. Eng Struct 2018;171:47–55. https://doi.org/10.1016/j.engstruct.2018.05.067.

[46] Buttlar WG, Hill BC, Kim YR, Kutay ME, Millien A, Montepara A, et al. Digital image correlation techniques to investigate strain fields and cracking phenomena in asphalt materials. Mater Struct Constr 2014;47:1373–90. https://doi.org/10.1617/s11527-014-0362-z.

[47] Correlated Solutions, Vic-2D, (2009) 59.

[48] Lakavath C, Joshi SS, Prakash SS. Investigation of the effect of steel fibers on the shear crack-opening and crack-slip behavior of prestressed concrete beams using digital image correlation. Eng Struct 2019;193:28–42. https://doi.org/10.1016/j.engstruct.2019.05.030.

[49] Crammond G, Boyd SW, Dulieu-barton JM. Speckle pattern quality assessment for digital image correlation. Opt Lasers Eng 2013;51:1368–78. https://doi.org/10.1016/j.optlaseng.2013.03.014.

[50] Lubliner J, Oliver J, Oller S, Onate E. A Plastic-Damage Model. Int J Solids Struct 1989;25:299–326.

[51] Lee J, Fenves GL. Plastic-Damage Model for Cyclic Loading of Concrete Structures. J Eng Mech 1998;124:892–900. https://doi.org/10.1061/(asce)0733-9399(1998)124:8(892).

[52] A. Gui T. Reference Abaqus GUI Toolkit Reference Manual Abaqus 6.11 GUI Toolkit Reference Manual, Dassault Syst Simulia Corp. Provid 2011 RI, USA.

[53] Malm R. Shear cracks in concrete structures subjected to in-plane stresses, Trita-Bkn. Bulletin of the Georgian Academy of Sciences 2006:136p.

[54] Al-Thairy H, Al-Jasmi SK. Numerical Investigation on the Behavior of Reinforced Lightweight Concrete Beams at Elevated Temperature, Iran. J. Sci. Technol. - Trans. Civ Eng 2021;45:2397–412. https://doi.org/10.1007/s40996-021-00580-4.

[55] Abbass W, Iqbal Khan M. Experimental and numerical investigation of flexural behavior of hybrid fiber reinforced high strength incorporating binary and ternary blend of ultra fines. Structures 2022;42:53–64. https://doi.org/10.1016/j.istruc.2022.05.116.

[56] IS 456, Plain Concrete and Reinforced, Bur. Indian Stand. Dehli. (2000) 1–114.